⌘ *Author's Choice*

A Polybasic Plasma Membrane Binding Motif in the I-II Linker Stabilizes Voltage-gated Ca$_V$1.2 Calcium Channel Function*

Gurjot Kaur[‡1], **Alexandra Pinggera**[‡1], **Nadine J. Ortner**[‡], **Andreas Lieb**[‡], **Martina J. Sinnegger-Brauns**[‡], **Vladimir Yarov-Yarovoy**[§], **Gerald J. Obermair**[¶], **Bernhard E. Flucher**[¶], **and Jörg Striessnig**[‡2]

From the [‡]*Institute of Pharmacy, Department of Pharmacology and Toxicology, and Center for Molecular Biosciences, University of Innsbruck, A-6020 Innsbruck, Austria, the* [§]*Department of Physiology and Membrane Biology, UC Davis School of Medicine, Davis, California 95616, and the* [¶]*Division of Physiology, Medical University of Innsbruck, A-6020 Innsbruck, Austria*

Background: L-type Ca^{2+} channels (LTCCs) are fine-tuned by different molecular mechanisms.
Results: Pore-forming α_1-subunits of LTCCs contain a polybasic amino acid sequence within their I-II linkers that binds to the plasma membrane. This polybasic motif is required for normal channel gating and modulation.
Conclusion: The polybasic cluster stabilizes normal channel activity.
Significance: We discovered a new modulatory domain of LTCCs within their pore-forming α_1-subunit.

L-type voltage-gated Ca^{2+} channels (LTCCs) regulate many physiological functions like muscle contraction, hormone secretion, gene expression, and neuronal excitability. Their activity is strictly controlled by various molecular mechanisms. The pore-forming α_1-subunit comprises four repeated domains (I–IV), each connected via an intracellular linker. Here we identified a polybasic plasma membrane binding motif, consisting of four arginines, within the I-II linker of all LTCCs. The primary structure of this motif is similar to polybasic clusters known to interact with polyphosphoinositides identified in other ion channels. We used *de novo* molecular modeling to predict the conformation of this polybasic motif, immunofluorescence microscopy and live cell imaging to investigate the interaction with the plasma membrane, and electrophysiology to study its role for Ca$_v$1.2 channel function. According to our models, this polybasic motif of the I-II linker forms a straight α-helix, with the positive charges facing the lipid phosphates of the inner leaflet of the plasma membrane. Membrane binding of the I-II linker could be reversed after phospholipase C activation, causing polyphosphoinositide breakdown, and was accelerated by elevated intracellular Ca^{2+} levels. This indicates the involvement of negatively charged phospholipids in the plasma membrane targeting of the linker. Neutralization of four arginine residues eliminated plasma membrane binding. Patch clamp recordings revealed facilitated opening of Ca$_v$1.2 channels containing these mutations, weaker inhibition by phospholipase C activation, and reduced expression of channels (as quantified by ON-gating charge) at the plasma membrane. Our data provide new evidence for a membrane binding motif within the I-II linker of LTCC α_1-subunits essential for stabilizing normal Ca^{2+} channel function.

Ca^{2+} influx through voltage-gated L-type Ca^{2+} channels (LTCCs)[3] is essential for many cellular events. It causes muscle contraction, initiates hormone secretion and neurotransmitter release, tunes neuronal excitability, and regulates gene expression (1, 2). LTCCs are large multiprotein complexes consisting of a pore-forming transmembrane α_1-subunit and accessory intracellular β- and extracellular $\alpha_2\delta$-subunits. To adapt Ca^{2+} entry to different cellular needs, functional diversity is achieved by multiple molecular mechanisms. Four different α_1-subunits (Ca$_V$1.1–1.4) can confer different biophysical properties (1) that are further adjusted by alternative splicing (3–5). In addition, the channels' accessory subunits tune their gating behavior and various protein interaction partners further provide LTCC currents with cell- and tissue-specific properties (1). However, rapid regulatory changes in current dynamics cannot be accomplished by changing channel composition. Instead, quick adaptive responses of channel activity require fast regulatory processes, including Ca^{2+} entry itself (inducing inactivation through channel-bound calmodulin (6)), phosphorylation by various kinases (7–9), extracellular pH (10), and direct G-protein modulation (11). Next to these mechanisms, membrane lipids are also important regulators of Ca^{2+} channel activity (12, 13). Depletion of phosphatidylinositol 4,5-bisphosphate (PIP$_2$) from the plasma membrane causes a rapid decrease of Ca^{2+} channel activity. In excised membrane patches, non-LTCC currents (Ca$_V$2.1 and Ca$_V$2.2) run down within minutes, which is attenuated by application of PIP$_2$ or its water-soluble analogue diC8-PIP$_2$ (14, 15). Rapid depletion of membrane PIP$_2$ content in intact cells by muscarinic 1 (M1) receptor activation, voltage-dependent phosphatases, or rapa-

---

mycin-induced translocation of inositol-lipid phosphatases confirmed the direct dependence of Ca_V1 ($Ca_V1.2$ and $Ca_V1.3$) and Ca_V2 ($Ca_V2.1$ and $Ca_V2.2$) channels on endogenous membrane PIP_2 (16). Channel inhibition by PIP_2 depletion occurs in a β-subunit-dependent manner because the β_{2a}-subunit, an isoform anchored to the plasma membrane by palmitoylation, attenuates inhibition (13, 17). Together with observations that arachidonic acid inhibits channel activity, a model has been proposed in which PIP_2, the fatty acid side chain of palmitoylated β_{2a}-subunits of voltage-gated Ca^{2+} channels (VGCCs), and arachidonic acid have overlapping binding sites, resulting in complex channel regulation by lipid metabolism (12, 17–19). There is also experimental evidence for more than one PIP_2 regulatory site in VGCCs: a higher affinity stimulatory "S" site supporting channel activity and a lower affinity inhibitory site ("R" site) stabilizing reluctant gating properties (12, 14, 20). Current working models suggest at least one facilitatory PIP_2 site on LTCCs and at least two on $Ca_V2.2$ channels (16).

Anionic phospholipids, like phosphatidylserine and phosphoinositides, target proteins with clusters of positive charges to the plasma membrane (21, 22). Despite unique insights into the structural basis of PIP_2 modulation within the crystal structure of K^+ channels (23, 24) and the identification of potential polyphosphoinositide binding domains within several ion channel proteins (for a review, see Refs. 13 and 25), the structural basis for fast modulation of VGCC function by plasma membrane lipids is unknown. It occurs at a very fast time scale, indicating that channel-lipid interactions are rapidly reversible and do not require more complex biochemical pathways, such as channel internalization (26). Similar to K^+ channels (23, 24), it appears likely that cytoplasmic domains located close to the plasma membrane participate in lipid interactions that stabilize channel function and allow modulation of channels by activation of phospholipase C (PLC). In addition to fast channel modulation, it is at present also unknown whether anionic lipids participate in the constitutive stabilization of VGCC function, which would be expected for very high affinity interactions not subject to regulation by changes in plasmalemmal phospholipid content (27).

Here we report the identification of a polybasic cluster within the cytoplasmic I-II linker of $Ca_V1.2$ α_1-subunits, which specifically binds to the plasma membrane. Activation of PLCs and polyphosphoinositide breakdown together with elevated intracellular Ca^{2+} levels reverse membrane binding. Four positively charged arginines are required for binding, most likely by strongly favoring a straight helix conformation of that region, positioning it entirely at the interface between the hydrocarbon core and lipid headgroups. Their neutralization in the intact channel facilitates channel opening and thus suggests a role of this polybasic cluster in stabilizing normal channel activity.

Experimental Procedures

All chemicals, reagents and antibodies were purchased from Sigma-Aldrich (Vienna, Austria) except where otherwise indicated. diC8-PIP_2 was purchased from Echelon Biosciences Inc. (Salt Lake City, UT).

Cloning of cDNA Constructs—The Ca_V α_1-subunits used in this study were identical with GenBank[TM] sequence accession numbers X05921 ($Ca_V1.1$ α_1), X15539 ($Ca_V1.2$ α_1), EU363339 ($Ca_V1.3$ α_1), and AJ224874 ($Ca_V1.4$ α_1).

For immunofluorescence experiments, Ca_V1 α_1 I-II linkers (amino acid numbering according to respective accession number: $Ca_V1.1$, 335–432; $Ca_V1.2$, 436–554; $Ca_V1.3$, 407–523; $Ca_V1.4$, 373–518) were cloned into vector pCIneo (Promega, E1841) in fusion with a FLAG tag at the C terminus. $Ca_V1.2$ I-II linker mutations were cloned into vector p3XFLAG-CMV-10 with a Myc tag at the C terminus and with a triple FLAG tag at the N terminus. The C terminus of $Ca_V1.3$ and the $Ca_V1.3$ W441A-I-II linker mutant were also cloned into vector p3XFLAG-CMV-10. $Ca_V1.2$ I-II linker mutations 4R4A and 4R4E were generated by splicing by overlap extension PCR (28) and cloned into vector mRFP-C1 with mRFP at the N terminus. Vector mRFP-C1 was generated by amplifying mRFP sequence from pCX-mRFP1 vector (29) to replace EYFP in pEYFP-C1 vector (Clontech, 6005-1). The C-terminally V5-tagged β-subunit β_{2a} (M80545), $_{C3S/C4S}\beta_{2a}$, and β_3 (NM_012828) constructs were expressed as described previously (30, 31).

The generation of N-terminally GFP-tagged β_3 (expression vector pCI-neo (Promega), generously provided by Manfred Grabner (32)) and C-terminally EGFP-tagged β_{2a}-subunits (expression vector pbA (33)) was described recently. mRFP-tagged pleckstrin homology (PH) domain of PLCδ (PH-PLCδ) was kindly provided by the Netherlands Cancer Institute (34). Untagged M1 receptor was generated from cyan fluorescent protein-labeled M1 receptor construct (generously provided by Stefan Böhm (Medical University of Vienna, Austria)) by restriction digestion and cloning into vector pCIneo. Peptide 526–554 with an N-terminal GFP tag ($_{GFP}526–554$) was generated by PCR cloning into vector EGFP (35). Lyn_{11}-FRB, mRFP-FKBP-pseudojanin, and GFP-PH-Osh2x2 constructs were kindly provided by Dominik Oliver and Gerald Hammond (36, 37). α_1-Subunit mutants $Ca_V1.2L_{4A}$ and $Ca_V1.2L_{4E}$ were generated by splicing by overlap extension-PCR and cloned into vector pCIneo. For short $Ca_V1.2$ α_1 mutations, $Ca_V1.2S_{4A}$ and $Ca_V1.2S_{4E}$, a stop codon was generated by PCR at position 1800 in the $Ca_V1.2$ α_1-subunit in pCIneo. The integrity of all constructs was confirmed by DNA sequencing (Microsynth, Eurofins).

Cell Culture and Transfection—For immunofluorescence microscopy, live cell imaging (LCI), and electrophysiology, tsA-201 cells were cultured in Dulbecco's modified Eagle's medium (DMEM), 10% fetal calf serum (Gibco, 10500.064), 2 mM glutamine (Sigma, G753) penicillin (10 units/ml), and streptomycin (10 μg/ml) and maintained at 37 °C in a humidified environment with 5% CO_2. Cells were grown and split when they reached about 80% confluence using 0.05% trypsin for cell dissociation. Cells were transiently transfected using Ca^{2+}-phosphate precipitation as described previously (38). For immunofluorescence and LCI, cells were replated 24 h after transfection onto 12 mm (for immunofluorescence) and 18 mm (for LCI) poly-L-lysine-coated coverslips and kept at 37 °C for 24–48 h until further experimentation. For whole-cell patch clamp recordings, tsA-201 cells were transiently transfected with equimolar ratios of cDNA encoding C-terminally long or short wild-type or mutant $Ca_V1.2$ α_1-subunits together with auxiliary β_3- (rat, NM_012828) and $\alpha_2\delta_1$- (rabbit, NM_001082276) sub-

units. To visualize transfected cells, GFP was co-transfected. Cells were then plated onto a 35-mm culture dish coated with poly-L-lysine. The cells were kept at 30 °C and 5% CO_2 and subjected to electrophysiological measurements about 48–72 h after transfection.

Immunofluorescence Microscopy—48 h after plating, tsA-201 cells were fixed in 4% (w/v) paraformaldehyde (Electron Microscopy Sciences, 15710) for 15 min at room temperature. Cells were washed thoroughly with phosphate-buffered saline and blocked for 30 min at room temperature with 5% (w/v) normal goat serum (GibcoBRL, 16210-064) in 0.2% (v/v) Triton/phosphate-buffered saline for cell permeabilization. Cells were incubated overnight at 4 °C with primary antibodies diluted in washing buffer containing 0.2% (v/v) Triton X-100 and 0.2% (w/v) BSA (immunoglobulin-free) in phosphate-buffered saline. After washing the cells in washing buffer, they were incubated with the secondary antibody for 1 h at room temperature in the dark. Washing was repeated, and the coverslips were mounted with Vectashield mounting medium (Vector Laboratories, H-1000) and sealed with nail polish on microscope slides. The following antibodies were employed: mouse monoclonal anti-V5, working dilution 1:500 (Invitrogen, R96025); rabbit polyclonal anti-FLAG (Sigma, F7425; 1:500); mouse monoclonal anti-FLAG (Sigma, F3165; 1:5000); Alexa Fluor-488-conjugated goat anti-rabbit and Alexa-594-conjugated goat anti-mouse antibodies (1:4000; Life Technologies, Invitrogen, A-11008 and A-11005). Images were captured with an Axiophot microscope (Carl Zeiss Inc., ×63, 1.4 numerical aperture Zeiss plan apochromat oil immersion lens) using a cooled CCD camera and at room temperature and Meta View image processing software (Universal Imaging Corp., West Chester, PA). Images were manually adjusted for brightness and contrast with Adobe Photoshop version 7.0.

Live Cell Imaging—After 24 h of replating, 18-mm coverslips containing live tsA-201 cells were washed once with Tyrode solution (130 mM NaCl, 2.5 mM KCl, 2 mM $CaCl_2$, 2 mM $MgCl_2$, 10 mM HEPES, 30 mM glucose, pH 7.4, 319 mosmol/liter), subsequently mounted on a Ludin chamber (Life Imaging Services) and kept in Tyrode solution until further processing. The chamber was placed on an ASI stage of an inverted Zeiss Axiovert 200M epifluorescence microscope (Carl Zeiss). Cells were imaged at room temperature. Different drugs (10 μM oxotremorine M, 50 μM m-3M3FBS (2,4,6-trimethyl-*N*-(meta-3-trifluoromethyl-phenyl)-benzenesulfonamide), 5 μM ionomycin, 20 μM wortmannin, 5 μM rapamycin (Calbiochem, Merck Millipore)) in different combinations (as indicated under "Results") were diluted to final concentrations in Tyrode solution and either directly added to the imaging chamber or added to a 35-mm culture dish containing the coverslip when preincubation was desired. Twelve-bit grayscale images were recorded at different time intervals using a cooled CCD camera (SPOT, Diagnostic Instruments), Metavue image processing software (Universal Imaging, Corp.), and a ×63, 1.4 numerical aperture Zeiss Plan Apochromat oil immersion lens. For presentation, selected images were linearly adjusted using Adobe Photoshop version 7.0 and CS4. For quantification, areas of interest of equal size were selected in the membrane, cytoplasm, and background of cells, and average pixel intensity was

recorded and used to calculate the membrane to cytoplasm ratio for every image. All quantitative data are represented as mean ± S.E. for the indicated number of experiments (*n*), except if stated otherwise. Data were analyzed by paired Student's *t* test, unpaired Student's *t* test, or one-way analysis of variance with Bonferroni post-hoc test using GraphPad Prism version 5.01 (GraphPad Software Inc.). Significance level was set to $p < 0.05$.

Electrophysiological Recordings—Whole-cell patch clamp experiments were performed in transiently transfected tsA-201 cells using an Axopatch 200B amplifier (Axon Instruments). Electrodes with a final resistance of 2–4 megaohms were pulled from borosilicate glass capillaries using a P-97 micropipette puller (Sutter Instruments) and subsequently fire-polished (MF-830 microforge, Narishinge). Ca^{2+} currents were measured using the following solutions: pipette solution, 135 mM CsCl, 10 mM Cs-EGTA, 1 mM $MgCl_2$, 10 mM HEPES, 4 mM Na_2-ATP, adjusted to pH 7.3 with CsOH; bath solution, 15 mM $CaCl_2$, 150 mM choline chloride, 1 mM $MgCl_2$, 10 mM HEPES adjusted to pH 7.3 with CsOH. All voltages were corrected for a junction potential of -9.3 mV. Recordings were digitized (Digidata 1322A digitizer, Axon Instruments) at 50 kHz, low pass-filtered at 5 kHz, and analyzed using pClamp version 10.2 software (Axon instruments). Current-voltage (*I-V*) relationships were obtained by applying a 20-ms square pulse protocol to various test potentials starting from a holding potential of -90 mV. Resulting *I-V* curves were fitted to Equation 1,

$$I = G_{max}(V - V_{rev})/(1 + \exp(-(V - V_{0.5})/k_{act})) \qquad \text{(Eq. 1)}$$

where *I* is the peak current amplitude, G_{max} is the maximum slope conductance, *V* is the test potential, V_{rev} is the extrapolated reversal potential, $V_{0.5}$ is the half-maximal activation voltage, and k_{act} is the activation slope. Channel inactivation was measured using a 300-ms pulse from a holding potential of -90 mV to V_{max}. For the estimation of the open probability (P_O), the area of the ON-gating current (Q_{ON}) was integrated and compared with the amplitude of the ionic tail current (I_{Tail}) at V_{rev}. Data were analyzed using Clampfit version 10.2 (Axon Instruments) and Sigma Plot 12 (Systat Software Inc.). To assess the effects of diC8-PIP_2 or the PLC activator m-3M3FBS, cells were depolarized from a holding potential of -90 mV to V_{max} for 20 ms at 0.1 Hz. As a control, $Ca_V1.2S$- or $Ca_V1.2S_{4E}$-expressing cells were perfused (flow rate: 250 μl/min) with bath solution only. To test whether diC8-PIP_2 can stabilize I_{Ca} decline, the same protocol was performed in the presence of 100 μM diC8-PIP_2 in the internal solution. DiC8-PIP_2 was prepared according to the manufacturer's instructions as a 1 mM stock in intracellular recording solution. Aliquots were kept frozen and diluted before use. To analyze the effects of phosphoinositide depletion on $Ca_V1.2$ currents, cells were perfused with 20 μM wortmannin and 50 μM m-3M3FBS. (flow rate: 250 μl/min). All quantitative data are represented as mean ± S.E. Statistical significance was determined by one- or two-way analysis of variance followed by Bonferroni post-hoc test or unpaired Student's *t* test as indicated using GraphPad Prism version 5.01 (GraphPad Software Inc.). Significance level was set to $p < 0.05$.

Rosetta Membrane Modeling of the Domain I-II Linker Region and Voltage-sensing Domain II of Ca$_V$1.2 Channel—Homology, *de novo*, and full-atom modeling of the voltage-sensing domain (VSD) of native and mutant Ca$_V$1.2 channels was performed using the Rosetta membrane method (39–41) and the x-ray structure of the bacterial voltage-gated Na$^+$ channel (Na$_V$Ab) VSD (42) as a template. Sequence alignment between native Ca$_V$1.2 and Na$_V$Ab VSDs shown in Fig. 8*A* was generated using the HHpred server (43, 44). The backbone structure of the transmembrane regions of Ca$_V$1.2 was built based on Na$_V$Ab VSD template. The 19-residue N-terminal region and S1-S2, S2-S3, and S3-S4 loops of Ca$_V$1.2 VSD were built *de novo* using the Rosetta cyclic coordinate descent loop modeling method (45) guided by membrane environment-specific energy function (39, 46). 10,000 models were generated for each Ca$_V$1.2 channel construct, and the top 10% of models ranked by total score were clustered (47) using root mean square deviation threshold that generates at least 150–200 models in the largest cluster. Models representing centers of the top five clusters and the best 10 models by total score were chosen for visual analysis. The top cluster and all 10 lowest energy models of native Ca$_V$1.2 showed very similar conformation of the domain I-II linker region (see Fig. 8). None of the top five clusters and 10 lowest energy models of alanine or glutamate mutants of Ca$_V$1.2 showed similar conformations of the domain I-II linker region (see Fig. 8). All structural figures were generated using the UCSF Chimera package (48).

Results

We (49) and others (50) have recently reported that the I-II linker of LTCC Ca$_V$1.3 and Ca$_V$1.2 α_1-subunits is targeted to the plasma membrane when expressed alone as a soluble protein in tsA-201 cells. Because the I-II linker harbors the high affinity interaction site for Ca^{2+} channel β-subunits (51), it is also capable of targeting co-expressed β-subunits to the plasma membrane, even in complex with β_1-subunit-bound Rab3-interacting molecule (49). Plasma membrane association of the linker is independent of β-subunits. Introduction of mutation W441A, which disrupts β-subunit binding to the linker (31, 52), prevented β-subunit targeting without affecting the plasma membrane localization of the linker (49). This suggested a specific, β-subunit-independent interaction of the I-II linker with the plasma membrane either through a membrane-associated protein or through direct interaction with membrane lipids.

I-II Linkers of All LTCC Isoforms Bind to the Plasma Membrane—To test whether plasma membrane binding is a property of all LTCC α_1-subunits, we transfected FLAG-labeled I-II linkers of Ca$_V$1.1, Ca$_V$1.2, Ca$_V$1.3, and Ca$_V$1.4 α_1-subunits (Fig. 1, *A–D, left*) into tsA-201 cells. Immunoblot analysis (not shown; $n = 3$) confirmed their expression as intact polypeptides. All LTCC I-II linkers were localized at the plasma membrane (Fig. 1, *A–D*). This localization pattern was independent of expression levels and indistinguishably observed in cells with weak and strong expression of the respective linkers (not shown). More than 85% of transfected cells (three independent experiments; 300 cells/experiment analyzed) showed this typical plasma membrane binding. In contrast, a FLAG-labeled control fragment derived from the Ca$_V$1.3 C terminus (FLAG-
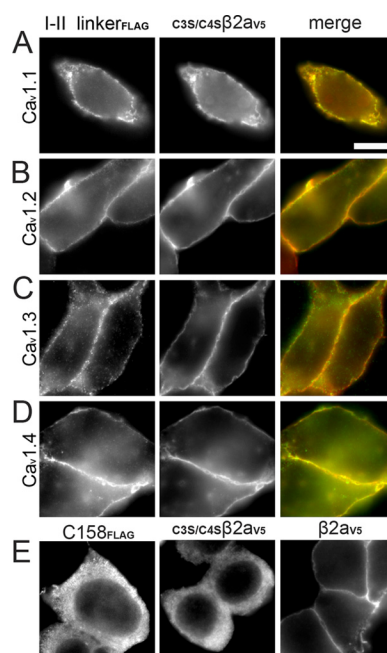

FIGURE 1. **All LTCC I-II linkers target to the plasma membrane in tsA-201 cells.** Immunofluorescence images of anti-FLAG-labeled LTCC (Ca$_V$1.1–Ca$_V$1.4) I-II linkers and anti-V5-labeled palmitoylation-deficient β_{2a} ($_{C3S/C4S}\beta2a_{V5}$) co-expressed in tsA-201 cells. *A–D, left*, anti-FLAG-labeled I-II linkers (I-II linker$_{FLAG}$); *middle*, anti-V5-labeled $_{C3S/C4S}\beta_{2a}$ ($_{C3S/C4S}\beta2a_{V5}$); *right*, merged images (*green*, anti-FLAG-labeled I-II linkers; *red*, anti-V5-labeled $_{C3S/C4S}\beta_{2a}$). *E*, expression of only anti-FLAG-labeled distal 158 amino acids of the Ca$_V$1.3 α_1 C terminus (C158$_{FLAG}$), of anti-V5-labeled $_{C3S/C4S}\beta2a_{V5}$, and of anti-V5-labeled palmitoylated β_{2a} ($\beta2a_{V5}$), respectively. Representative cells from three independent experiments are shown. *Scale bar*, 10 μm.

C158) clearly revealed a cytoplasmic distribution (Fig. 1*E, first panel*), as did the non-palmitoylated β_{2a} mutant $_{C3S/C4S}\beta_{2a}$ (Fig. 1*E, middle*). In contrast, normal palmitoylated β_{2a} revealed the expected plasma membrane targeting (Fig. 1*E, last panel*) and thus served as a positive control. Consistent with our previous findings, $_{C3S/C4S}\beta_{2a}$ ($n = 3$; Fig. 1, *A–D, middle panel*) and β_3 (not shown, $n = 3$) (49) also were localized at the plasma membrane after co-expression with one of the four LTCC I-II linkers. This shows that all LTCC I-II linkers support β-subunit plasma membrane targeting.

A Polybasic Cluster of Amino Acids Is Essential for I-II Linker Plasma Membrane Binding—To further identify the structural motif within the linker responsible for membrane targeting we expressed triple-FLAG-labeled linker peptides with deletions of equal size (29–30 amino acids) located in different parts of the Ca$_V$1.2 linker (Fig. 2*A*). The I-II linker of Ca$_V$1.2 was chosen for this analysis because it provided the best signal/noise ratio (not shown). Whereas membrane binding of mutants $\Delta436$–465, $\Delta466$–495, and $\Delta496$–525 remained unaffected by the deletions (Fig. 2*B*), removal of amino acids 526–554 (Fig. 2, *A* and *B*; $\Delta526$–554) abolished plasma membrane binding and resulted in cytoplasmic staining. Accordingly, mutants $\Delta436$–465 and $\Delta496$–525 translocated co-expressed $_{C3S/C4S}\beta_{2a}$ to the plasma membrane (Fig. 2*B*), whereas $\Delta526$–554 did not (Fig. 2*B*). Mutant $\Delta466$–495 failed to target $_{C3S/C4S}\beta_{2a}$ to the plasma membrane (Fig. 2*B*). This was expected, because the β-subunit α_1-subunit interaction domain (AID) is also removed by this deletion. By creating additional deletion mutants $\Delta536$–554 (no membrane binding; Fig. 3*A*) and $\Delta544$–554 (membrane-
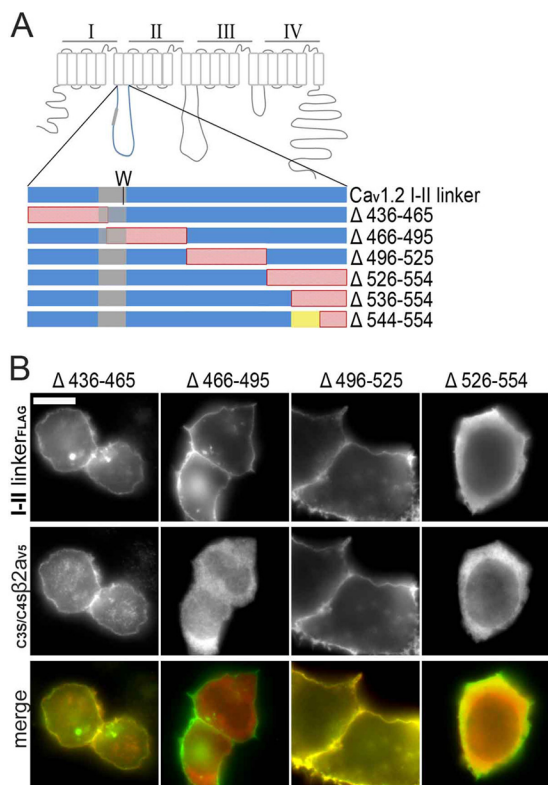
FIGURE 2. **Plasma membrane localizing signal is present in Ca$_V$1.2 I-II linker distal terminus.** *A*, schematic representation of all deletion mutants of the Ca$_V$1.2 I-II linker shown in *B*. A tryptophan residue (*W*) important for α_1-β subunit interaction marks the position of the AID domain (*gray*). *Red*, deletions; *yellow*, amino acids 536–544. *B*, immunofluorescence images of anti-FLAG-labeled deletion mutants of the Ca$_V$1.2 I-II linker (*top*), anti-V5-labeled $_{C3S/C4S}\beta_{2a}$ (*middle*), and merged images (*green*, anti-FLAG-labeled I-II linkers; *red*, anti-V5-labeled $_{C3S/C4S}\beta_{2a}$) co-expressed in tsA-201 cells. Representative images from three independent experiments are shown. *Scale bar*, 10 μm.

bound; Fig. 3*A*) we found that essential structural determinants for membrane targeting must be localized within positions 536–543 (Fig. 2*A*).

Secondary structure analysis of the Ca$_V$1.2 I-II linker using PSIPRED (53) (not shown) predicted the region between amino acids 531 and 550 to form a polybasic amphipathic α-helix with 8 of the 9 positive charges (Fig. 3*B*) located on one side of the helix as shown in a helical wheel plot (Fig. 3*B*). This included four arginines (Arg-537, Arg-538, Arg-541, and Arg-544) located within the region 536–544 required for membrane translocation (Fig. 3*C*, *yellow*), all of which are conserved among the I-II linkers of LTCCs (Fig. 3*D*). To test whether these positive charges are essential for plasma membrane binding, we neutralized them by mutations to alanines (mutant I-II-4R4A) or converted them to negatively charged glutamates (mutant I-II-4R4E; Fig. 3*C*). As expected, both mutations prevented the plasma membrane binding of the Ca$_V$1.2 I-II linker and of the co-expressed $_{C3S/C4S}\beta_{2a}$ subunits (Fig. 3*E*).

To assess whether this polybasic motif is sufficient to induce plasma membrane binding when attached to an otherwise cytoplasmic protein, we fused residues 526–554 to the C terminus of GFP ($_{GFP}$526–554; Fig. 3, *A* and *C*). This construct localized to the plasma membrane (Fig. 3*A*). It also accumulated in the nucleus of the vast majority of transfected cells. Notably, a distinct feature of lipid-interacting polybasic membrane targeting

motifs is their similarity to nuclear localization sequences (22), a property that may also account for the nuclear targeting of $_{GFP}$526–554. However, nuclear staining did not obscure plasma membrane binding (see also Figs. 4*A* and 5*B*), and this was also confirmed in dividing cells in which nuclear staining was completely absent (Fig. 3*A*, $_{GFP}$526–554, *right panel*; see also Fig. 5*A*). Taken together, these findings clearly demonstrate that positive charges at the C-terminal end of the Ca$_V$1.2 I-II linker form a plasma membrane binding motif sufficient for translocating the cytoplasmic I-II linker and fused GFP to the plasma membrane.

Involvement of Membrane Phosphoinositides in Plasma Membrane Targeting—The polybasic motif at the distal end of the I-II linker closely resembles clusters of positive charges found in other proteins, such as Rit and K-Ras (22) (Fig. 3*D*), and polybasic domains in other ion channels mediating protein-lipid interactions at the plasma membrane (for a review, see Ref. 13). We therefore hypothesized that this cluster of positive charges could serve a similar function. This notion was further supported by current folding models of Ca^{2+} channel α_1-subunits, which position these charges near the cytoplasmic end of the transmembrane helix IIS1 (42), which, in turn, places them in close proximity to the anionic lipids of the inner leaflet of the plasma membrane.

Many modulatory lipid interactions of ion channels involve polyphosphoinositides (13). Ca$_V$1 and Ca$_V$2 VGCCs are modulated by metabotropic receptors through activation of PLC, also independently of direct G-protein modulation (16). Activation of M1 receptors induces a partial inhibition of Ca^{2+} inward currents mostly by membrane depletion of PIP$_2$ in tsA-201 cells (16). This effect is mediated via activation of PLCβ (54). If binding of LTCC I-II linkers is dynamically regulated by interaction with PLC-metabolized polyphosphoinositides (primarily PIP$_2$), then it should be reversed in a PLC-sensitive manner.

We therefore co-transfected tsA-201 cells with M1 receptors and examined effects on membrane binding of our constructs in response to receptor activation with oxotremorine M (Oxo-M) using live cell imaging (Fig. 4, *A* and *B*). The PIP$_2$-specific mRFP-tagged pleckstrin homology domain of PLCδ (PH-PLCδ) served as positive control for monitoring PIP$_2$ breakdown (55). Oxo-M induced the relocation of PH-PLCδ but did not reverse the plasma membrane association of I-II linker-bound β_3-GFP ($n = 3$ independent experiments; Fig. 4*A*) or of $_{GFP}$526–554 ($n = 3$; Fig. 4*B*). Translocation of membrane-bound β_3-subunits was also absent in cells responding to co-transfected PH-PLCδ ($n = 3$), excluding a potential lack of Oxo-M action as a possible explanation. Even during prolonged observation times (10 min; not shown), no translocation was observed. As reported previously (55), Oxo-M-induced PIP$_2$ depletion was transient, resulting in a relocation of the PIP and PIP$_2$ biosensor GFP-PH-Osh2x2 (37) (5 of 21 cells) and PH-PLCδ (3 of 21 cells; not shown) within 2 min despite the continuous presence of Oxo-M. This is compatible with incomplete PIP/PIP$_2$ depletion in mammalian cells by Oxo-M (55) under these experimental conditions.

Previous studies have shown that plasma membrane targeting of cytoplasmic proteins through cationic motifs resembling
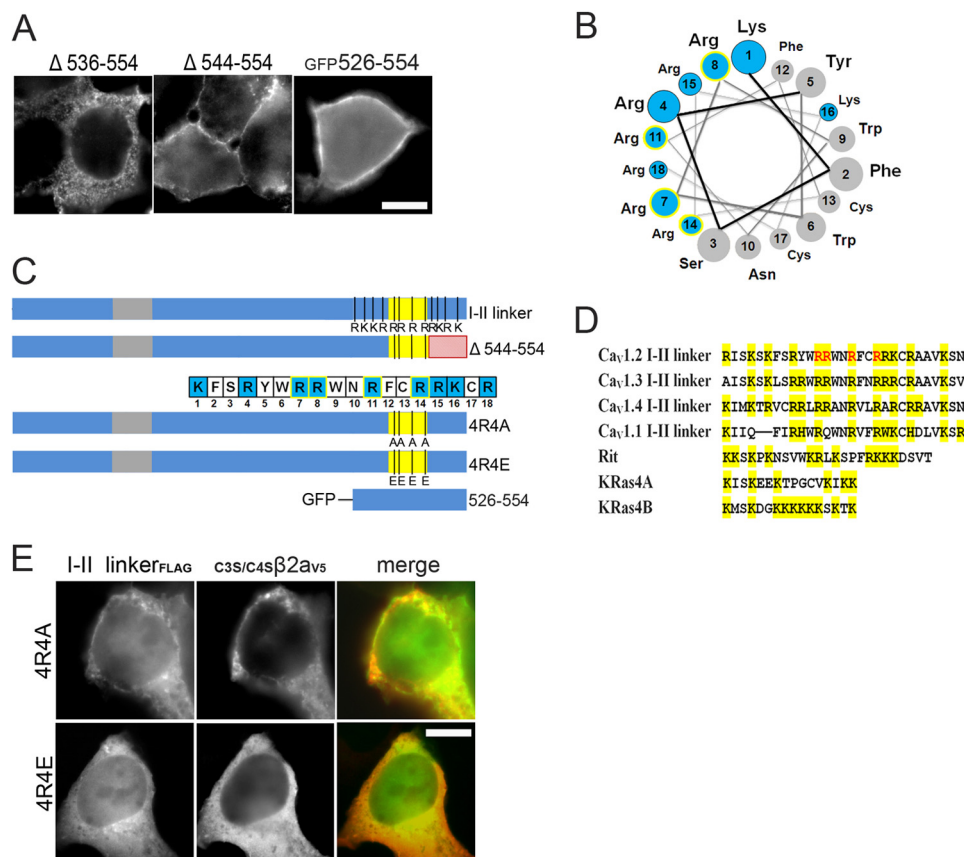
FIGURE 3. **Positively charged amino acids in region 536–544 are essential for $Ca_V1.2$ I-II linker targeting.** *A*, immunofluorescence images of anti-FLAG-labeled deletion mutants as indicated and of $_{GFP}526$–554. Staining of $\Delta536$–554 was always intracellular but with a granular appearance. This was only very rarely seen with $\Delta526$–554, which was typically of uniform distribution (*cf.* Fig. 2*B*). *B*, helical wheel representation of the proposed α-helix with positive charges indicated in *blue*. The 4 arginines important for membrane translocation are *highlighted* in *blue* with a *yellow outline* (*A* and *B*). *C*, schematic representation of positive residues (*R* and *K*) present in 526–554 sequence ($Ca_V1.2$ I-II linker). The four important arginines (Arg-537, Arg-538, Arg-541, and Arg-544) in amino acid sequence insert $\Delta544$–554 and mutations (4R4A and 4R4E) in the $Ca_V1.2$ I-II linker are indicated. GFP-tagged 526–554 is also shown. *Red*, deletion in 544–554; *yellow*, 536–544; *gray*, α_1-β subunit interaction site. *D*, putative phosphoinositide-binding domains of all LTCC I-II linkers are compared with published phosphoinositide-binding domains of Rit and K-Ras (22). All basic residues are *marked* in *yellow*, and ones that bind phosphoinositides are *highlighted* in *red*. *E*, immunofluorescence images of anti-FLAG-labeled charge neutralization linker mutants I-II 4R/4A and I-II 4R/4E (*left*), anti-V5-labeled $_{C3S/C4S}\beta_{2a}$ (*middle*), and *merged images* (*green*, anti-FLAG-labeled I-II linkers; *red*, anti-V5-labeled $_{C3S/C4S}\beta_{2a}$) expressed in tsA-201 cells. Representative images from three independent experiments are shown. *Scale bar*, 10 μm.

our polybasic sequence may also involve negatively charged lipids other than PIP_2, in particular PIP_3, PIP (22), or phosphatidylserine (21). We therefore used a rapamycin-inducible system (37) causing PIP and PIP_2 depletion. Briefly, RFP-tagged pseudojanin (PJ), an enzymatic chimera that converts PIP_2 to PIP and dephosphorylates PIP, was translocated from the cytosol to the plasma membrane upon rapamycin-induced Lyn_{11}-FRB interaction. Translocation of PJ to the plasma membrane started 15.6 ± 3.12 s after rapamycin application and was completed after 30.4 ± 3.61 s in the control experiments (Fig. 4, *C* and *D*). This was followed by membrane dissociation of co-transfected GFP-PH-Osh2x2 (starting 29.6 ± 4.03 s after drug administration, completed after 57.1 ± 3.28 s; mean $\pm$ S.E., $n = 24$). Notably, in 13 of 24 cells, some residual membrane staining of GFP-PH-Osh2x2 still remained (Fig. 4*C*). When we co-transfected the rapamycin-inducible system and the I-II linker together with β_3-GFP, PJ translocation started at 13.1 ± 1.43 s and was completed within 25.3 ± 1.07 s (mean $\pm$ S.E., $n = 16$) after rapamycin application. However, even after a prolonged recording time (20 min), we never observed a I-II linker-mediated translocation of β_3-GFP to the cytoplasm ($n = 16$ cells;

three independent experiments; Fig. 4*E*). We also combined the rapamycin-inducible system with wortmannin treatment. Preincubation with 20 μM wortmannin for 45–90 min before rapamycin application did not affect targeting of controls (PJ translocation started only upon rapamycin application after 20 ± 3.33 s, completion after 37.0 ± 5.17 s, $n = 10$) or linker-bound β_3-GFP ($n = 10$, three independent experiments; Fig. 4*F*).

Earlier studies have shown very strong plasma membrane binding of similar polybasic targeting motifs of small GTPases, such as Rit or K-Ras (21, 22) (Fig. 3*D*) or the plasma membrane targeting domain of RasGRP1, a Ras-specific exchange factor (56). Their dissociation requires, in addition to phosphoinositide hydrolysis, either depletion of PI3K products (22, 56) or prolonged elevation of intracellular Ca^{2+} (21). Because neither the rapamycin-inducible system nor the Oxo-M response appears to induce complete phosphoinositide depletion and induces no or, in the case of Oxo-M, only a transient intracellular Ca^{2+} signal (55), we employed the PLC activator m-3M3FBS together with wortmannin to induce PIP, PIP_2, and PIP_3 depletion and inhibit PI3K. m-3M3FBS activates PLCβ, -γ, and -δ isoforms and also induces a prolonged intracellular
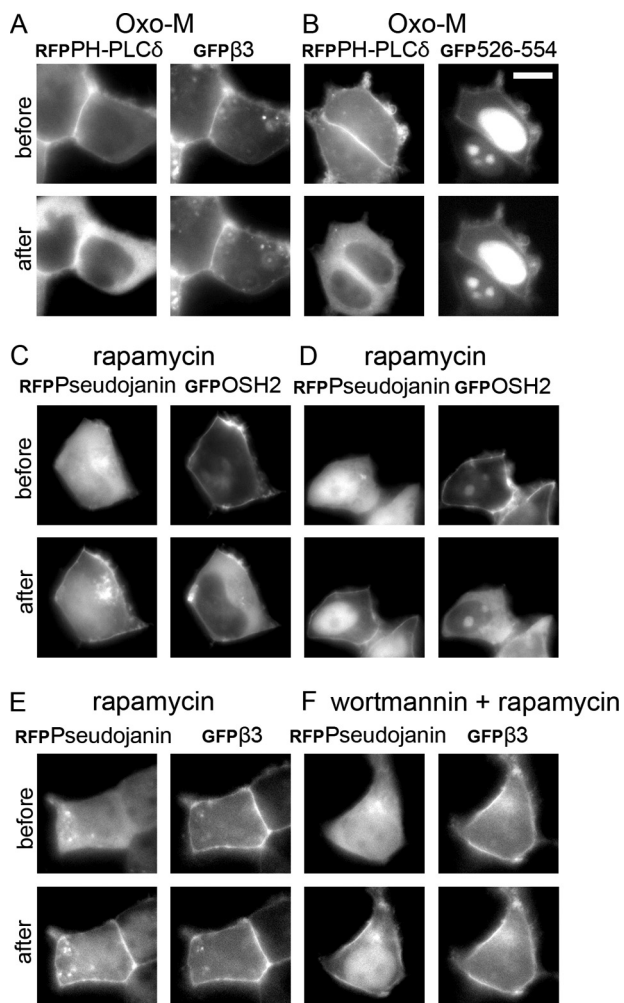
FIGURE 4. **Plasma membrane interaction of Ca$_V$1.2 I-II linker is not influenced by muscarinic receptor activation or rapamycin induced PIP or PIP$_2$ depletion.** *A* and *B*, mRFP-labeled PH-PLCδ and GFP-labeled β$_3$ with untagged Ca$_V$1.2 I-II linker or mRFP-labeled PH-PLCδ and GFP-labeled 526–554 were co-expressed with untagged muscarinic M1 receptor in tsA-201 cells and subsequently treated with the M1 receptor agonist Oxo-M (10 μM). Fluorescence was visualized using live cell imaging, and images before (t = 0 s) and after (t = 5 s) the drug application were recorded. *A*, *left*, mRFP-labeled PH-PLCδ; *right*, GFP-labeled β$_3$ in the same cells co-expressed with untagged Ca$_V$1.2 I-II linker and mRFP-labeled PH-PLCδ. *B*, *left*, mRFP-labeled PH-PLCδ; *right*, GFP-labeled peptide 526–554 in the same cells co-expressed with mRFP-labeled PH-PLCδ. Representative cells from three independent experiments are shown. *C–F*, cells co-transfected with Lyn$_{11}$-FRB, RFP-pseudojanin, and GFP-PH-Osh2x2 or Ca$_V$1.2 I-II linker together with β$_3$-GFP. Fluorescence was visualized before (t = 0 s) and after drug (t = 60 s) application. *C* and *D*, RFP-labeled pseudojanin (*left*) with GFP-labeled PH-Osh2x2 (*right*) as control before and after rapamycin treatment. Representative cells from eight independent experiments are shown. *E*, *left*, RFP-labeled pseudojanin; *right*, GFP-labeled β$_3$, before and after rapamycin application. Representative cells from three independent experiments are shown. *F*, *left*, RFP-labeled pseudojanin; *right*, GFP-labeled β$_3$ preincubated with wortmannin (*before*) and after the addition of rapamycin (*after*). Representative cells from three independent experiments are shown. *Scale bar*, 10 μm.

Ca^{2+} release (55, 57). Application of 50 μM m-3M3FBS alone was not sufficient to induce translocation within our observation period. However, co-application of m-3M3FBS together with wortmannin caused a delayed translocation of PH-PLCδ (n = 4; Fig. 5*A*, *left*) as well as of $_{GFP}$526–554 (n = 11 independent experiments; Fig. 5*A*, *right*) from the plasma membrane to the cytosol starting within a time frame of 20–30 min and completion in the following 7–10 min. This suggested a combined

effect of intracellular Ca^{2+} (which acts as a PLC co-activator (55)) and lipid hydrolysis for slow translocation. Accordingly, the addition of 5 μM ionomycin together with m-3M3FBS (58) induced an even faster relocation of PH-PLCδ to the cytoplasm (Fig. 5*B*, *left*). Translocation started 1.9 ± 0.2 min (mean ± S.D., n = 15) after m-3M3FBS/ionomycin stimulation and was complete within 45–55 s. When we treated cells co-transfected with the I-II linker together with β$_3$-subunits, PLC activation reversed the linker-mediated β$_3$-GFP association with the plasma membrane (Fig. 5*B*, *middle*). Although cell to cell differences for the translocation time course after adding m-3M3FBS/ionomycin were observed, the translocation of β$_3$-GFP and PH-PLCδ always occurred in parallel (n = 5 independent experiments; not shown). The GFP-tagged cationic peptide ($_{GFP}$526–554) also redistributed to the cytoplasm under these experimental conditions (n = 3; Fig. 5*B*, *right*). In contrast, no translocation was observed in control experiments with β$_{2aGFP}$ subunits, which are anchored to the membrane through palmitoylation, known to be insensitive to polyphosphoinositide breakdown (n = 6; Fig. 5*C*). Taken together, our data demonstrate that polyphosphoinositide breakdown as well as increased intracellular Ca^{2+} levels are required for unbinding of the distal portion of the Ca$_V$1.2 I-II linker from the plasma membrane.

*Role of the Polybasic Motif for Ca$_V$1.2 Channel Function and Modulation*—Due to the close proximity of the polybasic motif to the membrane and its lipid-dependent interaction with the plasma membrane, our data strongly suggest that this interaction also occurs in the pore-forming α$_1$-subunit of intact Ca$_V$1.2 channel complexes. We therefore introduced the mutations found to prevent membrane binding into the I-II linker constructs I-II-4R/4A and I-II-4R/4E (Fig. 3*D*) into the corresponding positions of the intact Ca$_V$1.2 α$_1$-subunits and expressed these mutants (together with β$_3$ and α$_2$δ$_1$) in tsA-201 cells. Mutation-induced changes of Ca^{2+} inward current (I_{Ca}) properties were then analyzed using whole-cell patch clamp experiments with Ca^{2+} as charge carrier. Ca$_V$1.2 α$_1$-subunit channels undergo partial proteolytic processing, giving rise to a C-terminally long (Ca$_V$1.2L) and short (Ca$_V$1.2S) variants. Both variants exist in the heart and brain and exhibit different current properties (59, 60). In particular, Ca$_V$1.2S exhibits a higher open probability (59, 60). We therefore tested the effects of the I-II linker mutations in both variants (long, mutants Ca$_V$1.2L$_{4A}$ and Ca$_V$1.2L$_{4E}$; short, mutants Ca$_V$1.2S$_{4A}$ and Ca$_V$1.2S$_{4E}$).

All four mutant constructs conducted inward Ca^{2+} currents. Current-voltage relationships revealed a significant 6–10 mV shift of $V_{0.5}$ in the hyperpolarizing direction for both mutants (Table 1 and Fig. 6*A*). This was due to a significant increase in the slope without changes in activation threshold (Table 1), suggesting more efficient coupling of pore opening to membrane depolarization. The mutations had little effect on the kinetics of I_{Ca} inactivation during 300-ms depolarizing pulses to the voltage corresponding to the peak of the *I-V* relationship (Table 2). The apparent reversal potential was also unchanged (Table 1). Differences between the mutants and wild-type channels were observed when we studied the relationship between the size of ON-gating charges (as a measure of active channels on the cell surface; enlarged ON-gating currents are
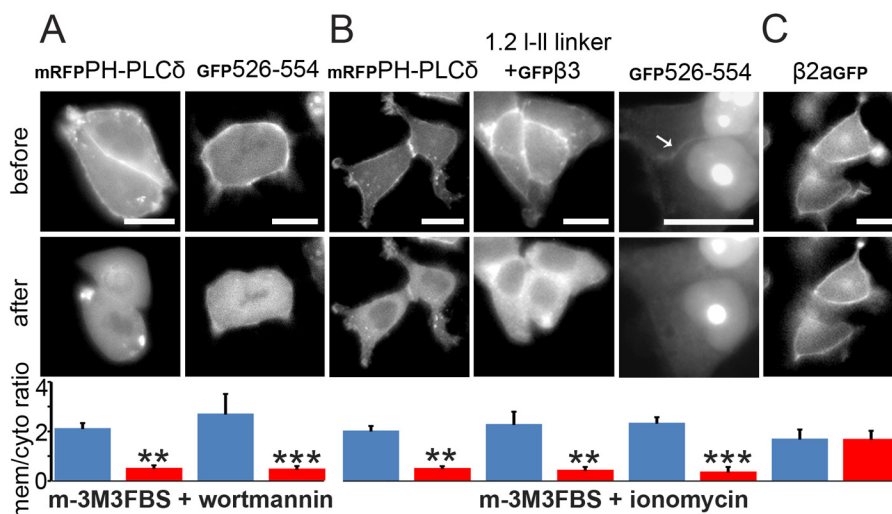
FIGURE 5. **Reversal of I-II linker-induced plasma membrane targeting due to phosphoinositide depletion accompanied by increased intracellular Ca^{2+} levels.** *A*, mRFP-labeled PH-PLCδ and GFP-labeled 526–554 were co-expressed with untagged muscarinic M1 receptor in tsA-201 cells treated with the PLC activator m-3M3FBS (50 μM) together with wortmannin (20 μM); *left*, mRFP-labeled PH domain of PLCδ; *right*, GFP-labeled 526–554. Representative cells from three independent experiments are shown. *B* and *C*, different constructs were expressed in tsA-201 cells and subsequently treated with the PLC activator m-3M3FBS (50 μM) and additional ionomycin (5 μM). *B*, *left*, mRFP-labeled PH-PLCδ; *middle*, GFP-labeled $β_3$-subunit co-expressed with $Ca_V1.2$ I-II linker; *right*, GFP-labeled peptide 526–554. The membrane-localized staining reversed by treatment is indicated by an *arrow*. Note that in the majority of cells, $_{GFP}526$–554 also showed strong nuclear targeting (for an explanation, see "Results"), which was absent in dividing cells without distinct nuclei (Figs. 3*A* and 5*A*). *C*, GFP-labeled $β_{2a}$ alone. To quantify the relocation from the membrane, pixel intensity from three representative areas of interest within the membrane of each cell were background-corrected, and the membrane/cytoplasm ratio was calculated from the means obtained before (*blue*) and after (*red*) PLC activation. Means ± S.E. (*error bars*) are shown for the indicated number of cells. Paired Student's *t* test was used. **, $p = 0.0049$ (PH-PLCδ, m-3M3FBS + wortmannin, $n = 3$); ***, $p = 0.00016$ (peptide 526–554, m-3M3FBS + wortmannin, $n = 3$); **, $p = 0.00427$ (PH-PLCδ, m-3M3FBS + ionomycin, $n = 15$); **, $p = 0.01087$ ($β_3$-subunit + $Ca_V1.2$ I-II linker, m-3M3FBS + ionomycin, $n = 5$); ***, $p = 0.0010$ (peptide 526–554, m-3M3FBS + ionomycin, $n = 3$); $p = 0.81799$ ($β_{2a}$, m-3M3FBS + ionomycin, $n = 6$). *Scale bar*, 10 μm.

TABLE 1

Biophysical properties of wild type and mutant $Ca_{V1.2L}$ and $Ca_{V1.2S}$

Parameters are indicated as means ± S.E. for a given number of experiments (*n*). Statistical significances are indicated for comparisons of $Ca_V1.2L$ *versus* $Ca_V1.2L_{4A}$ and $Ca_V1.2L_{4E}$ (*a–aaa*), $Ca_V1.2S$ *versus* $Ca_V1.2S_{4A}$ and $Ca_V1.2S_{4E}$ (*b–bbb*) (one-way analysis of variance, $Ca_V1.2L$: $V_{0.5}$ $p < 0.0001$, k_{act} $p < 0.0069$, I_{Tail}/Q_{ON} $p < 0.0001$; $Ca_V1.2S$: $V_{0.5}$ $p < 0.0016$, k_{act} $p < 0.0216$, P_o $p < 0.0001$; with Bonferroni post-hoc test as indicated in the table), and $Ca_V1.2L$ *versus* $Ca_V1.2S$ (*c–ccc*) (unpaired Student's *t* test). Significance was defined as $p < 0.05$ (*a*, *b*, and *c*), $p < 0.01$ (*aa*, *bb*, and *cc*), and $p < 0.001$ (*aaa*, *bbb*, and *ccc*). For reliable calculation of Q_{ON}, we omitted data from recordings in which Q_{ON} was not larger than 4-fold the signal of noise (5 of a total of 79 recordings).

$Ca_V1.2$ construct	$V_{0.5}$	Activation threshold	k_{act}	V_{rev}	n	$I_{Tail/QON}$	Q_{ON} mean (min; max)	n
	mV	*mV*	*mV*	*mV*		*ms⁻¹*	*pA*ms*	
$Ca_V1.2L$	13.96 ± 1.64	-31.58 ± 1.28	11.24 ± 0.45	77.08 ± 1.19	28	6.54 ± 0.47	260.5 (59.8; 565.4)	19
$Ca_V1.2L_{4A}$	3.47 ± 1.53^{aaa}	-33.40 ± 0.80	9.62 ± 0.24^a	73.56 ± 1.28	12	10.73 ± 1.36^{aa}	$127.5 (57.4; 224.7)^a$	9
$Ca_V1.2L_{4E}$	4.07 ± 1.90^{aa}	-30.81 ± 1.59	9.30 ± 0.34^a	77.72 ± 2.16	11	14.00 ± 1.27^{aa}	$100.4 (40.1; 317.8)^{aa}$	9
$Ca_V1.2S$	7.03 ± 1.41^{cc}	-32.09 ± 0.81	10.06 ± 0.38	77.20 ± 1.28	22	13.35 ± 1.46^{cc}	266.2 (101.2; 674.7)	12
$Ca_V1.2S_{4A}$	0.77 ± 1.22^{bb}	-32.63 ± 0.72	8.95 ± 0.28^b	76.69 ± 1.18	22	22.90 ± 2.21^{bb}	$136.1 (46.4; 495.7)^b$	14
$Ca_V1.2S_{4E}$	1.31 ± 1.28^{bb}	-31.92 ± 0.73	8.85 ± 0.34^b	74.46 ± 1.17	17	31.42 ± 2.07^{bbb}	$76.4 (40.0; 172.0)^{bbb}$	11

shown in the *insets* of Fig. 6*B*) and the size of ionic tail currents (Fig. 6*B*). As shown by us and others previously, this ratio provides an estimate for the channel's open probability (61–63). The two wild-type constructs served as an internal control because a higher open probability was reported earlier for $Ca_V1.2S$ (59, 61). This is evident as a statistically significant difference of the I_{Tail}/Q_{ON} ratio in our experiments (Fig. 6*B*; see Table 1 for statistics). This is also evident from the steeper slopes of the regression lines of plots of I_{Tail} *versus* Q_{ON} (Fig. 6*C*). In $Ca_V1.2L$, the 4R/4A mutation caused a 64% increase in the I_{Tail}/Q_{ON} ratio. A similar increase was also observed in the $Ca_V1.2S$ mutants despite higher basal open probability. An even larger effect was seen for the $Ca_V1.2L_{4E}$ and $Cav1.2S_{4E}$ mutants, which more than doubled the open probability. We also found that all four arginine mutant constructs significantly reduced Q_{ON} in both $Ca_V1.2L$ and $Ca_V1.2S$, with the reduction again more pronounced for the two 4R/4E mutations. Our data

demonstrate that positive charges located in proximity to the transmembrane segment IIS1 within the I-II linker are important determinants of normal $Ca_V1.2$ Ca^{2+} channel function independent of the length of their C-terminal tails and basal open probabilities. The negative shift in $V_{0.5}$ and higher open probability both indicate a tighter coupling between the voltage sensor and the pore. Based on our membrane targeting analysis, we propose that we have identified a site that is involved in the membrane lipid-dependent stabilization of channel function as well as the regulation of the expression of functional channels at the plasma membrane.

We also tested whether the arginine mutations in $Ca_V1.2S_{4E}$ (*versus* $Ca_V1.2S$ as wild-type control) affect the time-dependent decline of whole-cell I_{Ca} and the modulation by added PIP_2 (by intracellular application of a 100 μM concentration of the water-soluble PIP_2 analogue diC8-PIP_2, (15, 64)) or phosphoinositide hydrolysis induced by wortmannin (20 μM) plus
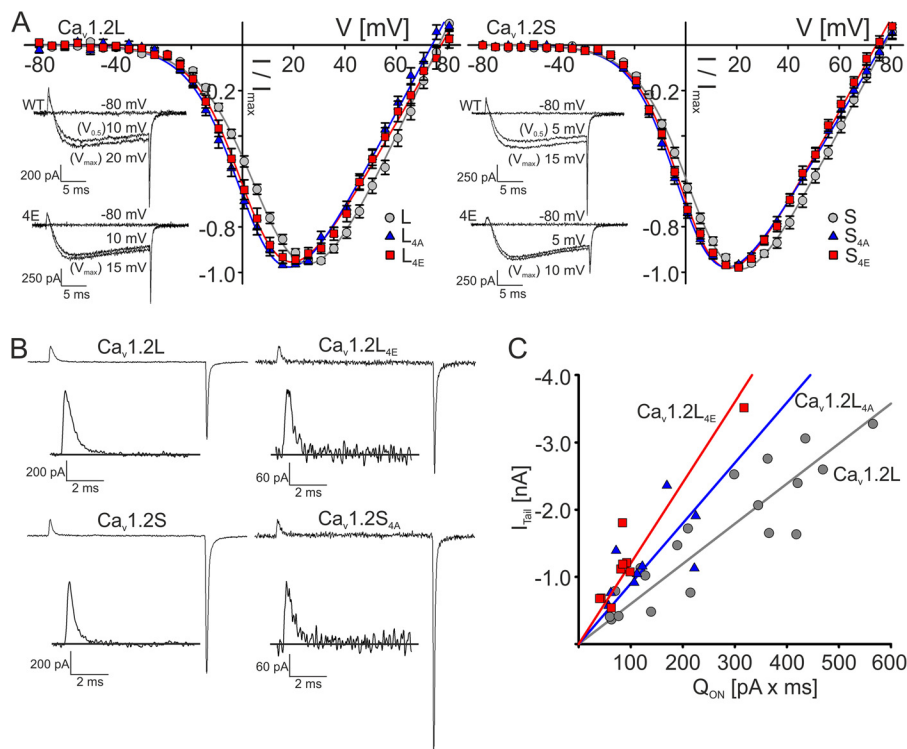
FIGURE 6. **Biophysical properties of wild-type and mutant Ca$_V$1.2L and Ca$_V$1.2S.** Parameters and statistics are given in Table 1. *A*, normalized current-voltage (*I-V*) relationships of Ca$_V$1.2L (*gray circles*), Ca$_V$1.2L$_{4A}$ (*blue triangles*), and Ca$_V$1.2L$_{4E}$ (*red squares*) (*left*) and Ca$_V$1.2S (*gray circles*), Ca$_V$1.2S$_{4A}$ (*blue triangles*), and Ca$_V$1.2S$_{4E}$ (*red squares*) (*right*) measured by a 20-ms depolarization step to various test potentials using 15 mM Ca^{2+} as a charge carrier. Data points are represent means ± S.E. (*error bars*). *Insets*, representative traces for Ca$_V$1.2L (*top left*), Cav1.2L$_{4E}$ (*bottom left*), Cav1.2S (*top right*), and Ca$_V$1.2S$_{4A}$ (*bottom right*) for the indicated voltages. Note that at test potentials close to the $V_{0.5}$ of wild-type channels, the mutant channels exhibit current amplitudes closer to V_{max} due to a shift of the *I-V* relationship toward more negative voltages. *B*, representative current traces of Ca$_V$1.2L (*top left*) versus Ca$_V$1.2L$_{4E}$ (*top right*) and Ca$_V$1.2S (*bottom left*) versus Ca$_V$1.2S$_{4A}$ (*bottom right*) obtained by depolarizing the cell from −90 mV to V_{rev}. *Insets*, enlarged Q_{ON} of the *traces*. *C*, correlation of Q_{ON} (area) with maximum tail current amplitude (I_{Tail}) measured at V_{rev} for wild-type and mutant Ca$_V$1.2S. The *color code* is as in *A*. The following slopes were obtained by linear regression analysis: −12.2 ± 1.13 for Ca$_V$1.2S ($R^2 = 0.64$), −17.2 ± 1.14 for Ca$_V$1.2S$_{4A}$ ($R^2 = 0.82$), −27.7 ± 1.73 for Ca$_V$1.2S$_{4E}$ ($R^2 = 0.70$). Slopes were significantly different for each data set ($p < 0.0001$; F-test: F (DFn, DFd) = 15.6 (2, 34)) as well as for Ca$_V$1.2L and corresponding mutants ($p < 0.0001$; not shown).

TABLE 2

Inactivation properties of wild-type and mutant Ca$_{V1.2}$L and Ca$_{V1.2}$S

Cells were depolarized for 300 ms from a holding potential of −90 mV to V_{max}. *R* values represent the remaining fraction of I_{Ca} (15 mM) after 50, 100, or 250 ms. Parameters are indicated as means ± S.E. for a given number of experiments (*n*). Statistical significances are indicated for comparisons of Ca$_V$1.2L *versus* Ca$_V$1.2L$_{4A}$ and Ca$_V$1.2L$_{4E}$ (*a*) (one-way analysis of variance with Bonferroni post-hoc test as indicated in the table) and Ca$_V$1.2L *versus* Ca$_V$1.2S (*b* and *bb*, unpaired Student's *t* test). Significance was defined as $p < 0.05$ (*a* and *b*) and $p < 0.01$ (*bb*).

Ca$_V$1.2 construct	R50	R100	R250	n
	%	%	%	
Ca$_V$1.2L	65.01 ± 2.51	49.39 ± 2.61	32.54 ± 2.02	7
Ca$_V$1.2L$_{4A}$	60.77 ± 2.05	46.83 ± 2.23	33.16 ± 2.34	7
Ca$_V$1.2L$_{4E}$	56.96 ± 1.67[a]	42.60 ± 2.43	29.83 ± 1.64	7
Ca$_V$1.2S	52.86 ± 2.37[bb]	37.09 ± 2.02[bb]	24.72 ± 2.02[b]	13
Ca$_V$1.2S$_{4A}$	50.63 ± 2.57	36.32 ± 2.31	26.48 ± 2.18	13
Ca$_V$1.2S$_{4E}$	52.28 ± 2.46	38.55 ± 2.36	27.22 ± 2.14	13

m-3M3FBS (50 μM) as in live cell imaging experiments (Fig. 5*A*). Perfusion of cells with control solution induced a slow decrease in activity with time ("run-down"), as expected for Ca$_v$1.2 channels (65). I_{Ca} decline during perfusion with control solution was similar in wild-type and the mutant channel and was also not affected by intracellular application of diC8-PIP$_2$ (Fig. 7). However, extracellular perfusion with wortmannin/m-3M3FBS significantly inhibited I_{Ca} of wild-type and Ca$_v$1.2$_{4E}$ channels, but this current inhibition was significantly attenuated in the mutant channel (Fig. 7). This indicates that membrane association of the distal I-II linker through its positive charges not only stabilizes a more reluctant channel state (Fig. 6) but also weakens inhibition of channel activity by phosphoinositide depletion.

*Structural Modeling of the Domain I-II Linker Region of Ca$_V$1.2 Channel*—To further explore the conformation of this distal domain I-II linker region of the Ca$_V$1.2 channel (corresponding to residues 536–554 containing the polybasic cluster), its interaction with the inner leaflet of the membrane bilayer, and potential changes introduced by charge neutralizations, we applied the Rosetta membrane method (39–41) and the x-ray structure of the voltage-sensing domain of a recently crystallized bacterial voltage-gated Na$^+$ channel, Na$_V$Ab (Fig. 8*A*) as described under "Experimental Procedures." The best models of the native Ca$_V$1.2 channel revealed convergence between the top cluster model (the most frequently sampled conformation) and the 10 lowest energy models (Fig. 8*B*). In those models, the distal I-II linker forms a straight helix in
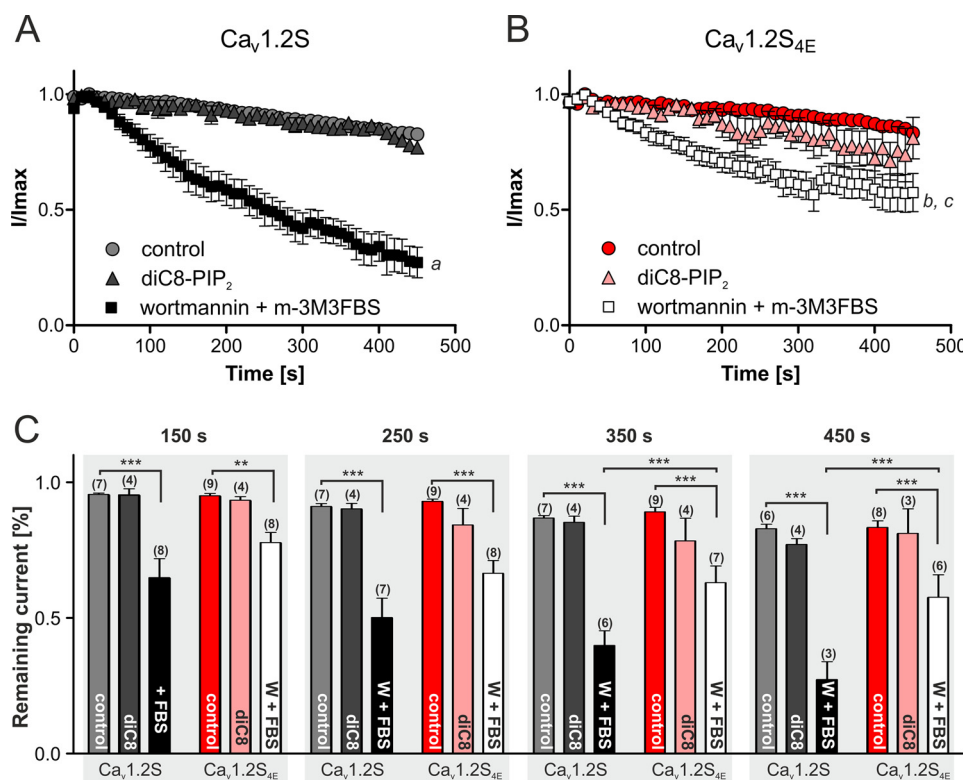
IGURE 7. **Modulation of $Ca_V1.2S$ and $Ca_V1.2S_{4E}$ currents by wortmannin/m-3M3FBS or diC8-PIP$_2$ treatment.** *A*, $Ca_V1.2S$, perfused with bath solution (control; *gray circles*; data are shown for seven cells; due to different recording duration, means $\pm$ S.E. reflect $n = 7$ until 410 s, $n = 6$ until 450 s), 100 μM intracellular diC8-PIP2 (*gray triangles*; means $\pm$ S.E., $n = 4$), or extracellular 20 μM wortmannin and 50 μM m-3M3FBS (*black squares*; means $\pm$ S.E. for $n = 8$ until 280 s, $n = 3$ until 450 s). *B*, $Ca_V1.2S_{4E}$, control (*red circles*; $n = 9$ cells until 440 s, $n = 8$ cells until 450 s), 100 μM intracellular diC8 (*red triangles*; $n = 4$ until 420 s, $n = 3$ until 450 s), or extracellular 20 μM wortmannin and 50 μM m-3M3FBS (*white squares*; $n = 8$ until 320 s, $n = 6$ until 450 s). Statistical analysis was performed using two-way analysis of variance of all data sets followed by Bonferroni post hoc test. Wortmannin/m-3M3FBS treatment significantly enhanced current decrease over time for both constructs (*a*, $p < 0.01$ after 100 s and $p < 0.001$ after 120 s for $Ca_V1.2S$; *b*, $p < 0.05$ after 140 s and $p < 0.001$ after 170 s for $Ca_V1.2S_{4E}$). The wortmannin/m-3M3FBS response was significantly attenuated in $Ca_V1.2S_{4E}$ *versus* wild type (*c*, $p < 0.05$ after 260 s, $p < 0.01$ or $p < 0.001$ after 330 s). DiC8-PIP2 treatment had no effect and was also not different between wild type and mutant $Ca_V1.2$. Because current underwent some minor initial run-up, time 0 was set when the currents reached a stable maximum (1.5–2 min after start of perfusion) to which current amplitudes were normalized. *C*, percentage of remaining current of $Ca_V1.2S$ and $Ca_V1.2S_{4E}$ in control-, diC8-, or wortmannin/m-3M3FBS (*W/FBS*)-treated cells after different time points. Data are shown as mean $\pm$ S.E. (*error bars*). Statistical significance at the indicated time points was taken from the statistical analysis described above. *, $p < 0.05$; **, $p < 0.01$; ***, $p < 0.001$.

which arginine residues are oriented away from the hydrophobic layer of the membrane (*lines* in Fig. 8) and are therefore in a favorable position for possible interactions with lipid phosphate groups (Fig. 8*C*). Large hydrophobic residues in the domain I-II linker region are oriented toward the hydrophobic layer of the membrane, which is in good agreement with their favorable environment based on analysis of available membrane protein structures (Fig. 8*D*). The best models of the domain I-II linker arginines mutated to alanines or glutamates are shown in Fig. 8, *E* and *F*. Unlike in wild-type models, there is no convergence among any of the top cluster models and the best scoring models. Our model suggests that native arginines in the distal I-II linker strongly favor straight helix conformation, positioning it entirely at the interface between the hydrocarbon core and lipid head groups.

Based on Rosetta predictions, the alanine mutations clearly disturb this conformation, making the helical region structurally unstable. We therefore suggest that alanine and glutamate mutations in the domain I-II linker not only affect its plasma membrane binding but also disturb secondary structure, leading to altered positioning of the domain I-II linker helix near the membrane-spanning helices of repeat II.

Discussion

We describe the identification of a polybasic motif within the I-II linker of the pore-forming α_1-subunit of voltage-gated $Ca_V1.2$ L-type Ca^{2+} channels with biochemical features that allow its attachment to the inner leaflet of the plasma membrane via interaction with negatively charged phospholipids. First, we demonstrate that the I-II linkers of all four LTCC isoforms bind to the plasma membrane in living cells (Fig. 1). This enables this polypeptide to translocate large complexes of cytoplasmic proteins to the plasma membrane (different β-subunits, Rab3-interacting molecule in complex with β-subunits (49)). Second, this interaction is reversible upon pharmacological activation of PLC together with either Ca^{2+} as an additional PLC activator (66) or with wortmannin (Fig. 5), which prevents resynthesis of polyphosphoinositides (22). Under both activating conditions, the time course of membrane unbinding of the I-II linker closely follows the time course of unbinding of the PIP$_2$-selective sensor PH-PLCδ. No such translocation was found for β_{2a}-subunits, which are membrane-anchored through their palmitoic acid side chain and thus insensitive to PLCs. Together, these findings provide
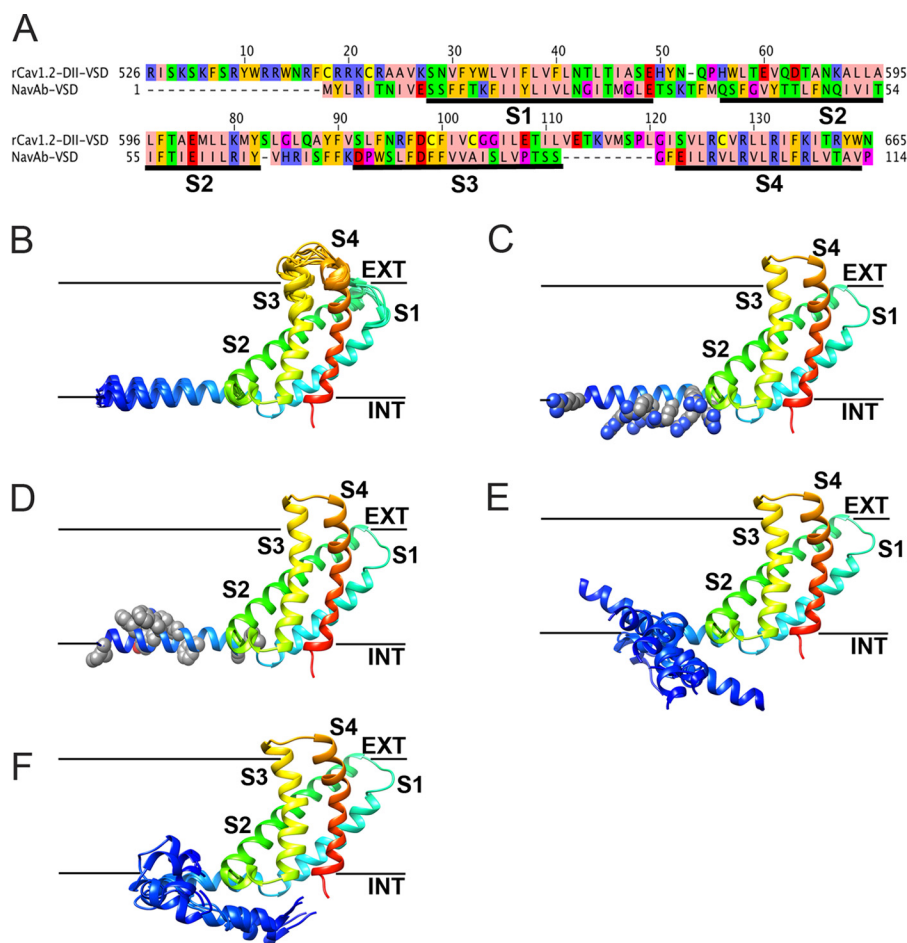
FIGURE 8. **Structural models of the domain I-II linker region of native Ca$_V$1.2 channel.** *A*, sequence alignment between the native Ca$_V$1.2 I-II linker region and the domain II voltage-sensing domain (*rCa$_V$1.2-DII-VSD*) and *Na$_V$Ab* voltage-sensing domain (*Na$_V$Ab-VSD*). Transmembrane segments S1–S4 are *underlined* by *black bars* and *labeled*. Amino acids were colored using the Zappo color scheme in Jalview. *B–D*, transmembrane view of the *ribbon representation* of the top cluster models of the VSD of Ca$_V$1.2 with the 10 lowest energy Rosetta models superimposed in *B* and *space-filling representations* of arginine side chains in the domain I-II linker helix in *C* and of large hydrophobic side chains in the I-II linker helix in *D*. *E* and *F*, *transmembrane view* of *ribbon representation* of the top five clusters and 10 lowest energy Rosetta models of the Ca$_V$1.2 VSD of alanine mutants superimposed in *E* and of glutamate mutants superimposed in *F*. Models are *colored* in a *rainbow scheme* from *blue* (N-terminal region before S1 segment) to *red* (S4 segment). Transmembrane segments S1–S4 are labeled accordingly. *Black bars*, approximate location of the extracellular and intracellular edges of the hydrophobic layer of the membrane.

strong experimental evidence that binding of the I-II linker through this polybasic motif to the plasma membrane also involves interaction with polyphosphoinositides. Third, the primary structure of our lipid-binding motif has the characteristics of previously reported polybasic motifs implicated in polyphosphoinositide-interactions of other ion channels or of small GTPases, such as Rit and K-Ras (Fig. 3C) (22). The polybasic motifs of these proteins are sufficient for their plasma membrane targeting. Similar to our motif, the removal of only a few residues in Rit was sufficient to completely prevent translocation (3 in Rit, 4 in the I-II linker) (22). Moreover, positively charged clusters required for interaction with membrane lipids have recently also been identified in the auxiliary β_{2e} subunit of VGCC (67).

Using *de novo* molecular modeling, we predict this membrane binding motif to form a straight α-helix positioned entirely at the interface between the hydrocarbon core and lipid headgroups, with the positive charges facing the lipid phosphates. Moreover, according to the model, the four arginines not only support plasma membrane binding of the I-II linker but are also necessary to stabilize this secondary structure in the

context of the membrane environment. This stabilization may also explain the functional changes we observed. We demonstrate that the four basic residues are by themselves determinants of Ca$_V$1.2 Ca^{2+} channel function. In two different Ca$_V$1.2 α_1-subunit variants with distinct intrinsic open probabilities (61), neutralization of these charges enhanced Ca$_V$1.2-mediated inward currents resulting from increased tail Ca^{2+} currents relative to total ON-gating charge. In addition, these mutations also shifted half-maximal activation to more negative potentials by increasing the slope of the current-voltage relationship. Both observations indicate that charge neutralization (or conversion) enhances the coupling between voltage sensing and pore opening. This is in accordance with the previous finding that the I-II linker encodes self-reliant molecular motifs for channel activation independent of β-subunits (68, 69). Our data show that residues remote from the β-subunit interaction site in the I-II linker are required for stabilization of normal Ca$_V$1.2 channel function. Although only crystallization studies such as those recently described for Kir2.2 and GIRK2 K$^+$ channels (23, 24) can ultimately confirm the direct interaction of channel domains with membrane lipids, our data pro-

vide strong evidence that the polybasic motif described here constitutively stabilizes channel function through membrane lipid binding. In addition, we also found that charge neutralization and conversion also reduced Q_{ON}, revealing a reduction of functional channels at the plasma membrane. This strongly indicates that the interaction of this basic motif with negatively charged membrane lipids is also important for regulating the expression of functional $Ca_V1.2$ channels at the membrane surface.

Previous studies have identified other potential PIP_2 interaction sites within VGCC α_1-subunits. Mutation of Ile-1520 in segment IIIS6 of the $Ca_V2.1$ α_1-subunit reduced current rundown attributed to PIP_2 depletion (70), thus proposing a channel-stabilizing PIP_2 interaction with a region close to the pore. The C terminus of the $Ca_V2.1$ α_1-subunit has also been implicated in a PIP_2-dependent regulation of the direct (and voltage-dependent) inhibition of $Ca_V2.1$ channels by receptor-mediated G-protein activation. Evidence has been provided that this could be due to PIP_2-mediated interaction with the plasma membrane because the C-terminal channel fragment showed binding to polyphosphoinositide strips *in vitro* (71). However, the polybasic cluster implicated in this interaction is not present in the C termini of LTCCs.

So far, we could not obtain evidence that the polybasic binding motif identified here is also important for the dynamic regulation of channel function by physiological modulatory pathways inducing phospholipid breakdown. Although we can show breakdown of PIP_2 in our transfected cells by activation of M1 receptors robust enough to induce cytoplasmic relocation of the PIP_2-selective probe PH-PLCδ, this did not result in relocation of our I-II linker constructs. In electrophysiological studies, Oxo-M stimulation of tsA-201 cells transfected with M1 receptors and $Ca_V1.2$ induces a 33–60% inhibition of Ba^{2+} currents through $Ca_V1.2$ (16), and more than half of this modulation is dependent on PIP_2. This is compatible with models predicting that under these experimental conditions, 1–7% of the total PIP_2 and 12–40% of PIP remain non-hydrolyzed in these cells (55). This may be sufficient for maintaining the binding of the I-II linker during stimulation with Oxo-M. Indeed, it is known from studies with proteins containing polybasic targeting motifs, similar to the one described here in the I-II linker, that efficient plasma membrane unbinding requires more than just PIP_2 hydrolysis. The GTPases Rit and K-Ras require complete depletion of both PIP_2 and PIP or PI3K products. Binding still persists when only one of them is depleted (22, 37). This is also in accordance with a previous study that observed that complete loss of the binding of the RasGRP1 plasma membrane targeting domain only occurred after combined treatment with the PLC activator m-3M3FBS and wortmannin and not with m-3M3FBS alone (56). In our experiments, dissociation of the $Ca_V1.2$ I-II linker from the plasma membrane was also achieved by combining m-3M3FBS with ionomycin-induced Ca^{2+} increase. This suggests that Ca^{2+} also plays a role in this mechanism. Thus, it requires a second mechanism that either further enhances polyphosphoinositide breakdown (wortmannin) or a strong intracellular Ca^{2+} signal.

The requirement of Ca^{2+} could also indicate that PLCδ or phosphatidylserine plays a major role in reversing the plasma membrane targeting of the $Ca_V1.2$ I-II linker. PLCδ is mainly activated by an increase in intracellular Ca^{2+} levels (10–100 nM), usually due to prior activation of other PLCs (72–74). Moreover, it has been shown that sustained Ca^{2+} increase can cause phosphatidylserine externalization (75). The observed translocation of the I-II linker upon m-3M3FBS and ionomycin application could therefore also be due to dissociation from the negatively charged phosphatidylserine. Hence, we propose that the I-II linker can interact with phosphoinositides as well as with phosphatidylserine, which has also been reported for Ras-GRP1 plasma membrane targeting (56). Independent of the exact mechanism, our biochemical studies provide evidence for a strong and constitutive binding of the polybasic membrane binding motif identified here, which may involve different negatively charged phospholipids.

The observation of facilitated gating and enhanced Ca^{2+} influx in our channel mutants is unexpected because recent work (76) has demonstrated inhibition of channel activity by M1 receptor-activated PIP_2 breakdown. We were unable to test the effects of our mutations on M1 receptor-induced channel inhibition because the co-transfection was toxic for the cells and precluded their use in patch clamp recordings. Instead, we show that inducing phosphoinositide breakdown by treatment of cells with wortmannin and the PLC activator m-3M3FBS causes the expected inhibition of current amplitude but that this response is significantly attenuated by disruptive mutations in the polybasic motif as shown for $Ca_V1.2S_{4E}$ (Fig. 7). This further supports our interpretation that this membrane binding motif not only stabilizes a more reluctant gating mode but also supports moderation of channel activity by lipid breakdown once targeted to the plasma membrane.

The lipid-binding motif described here is positioned on the C-terminal end of the I-II linker. In contrast to the N-terminal half of the linker, this region has not previously been implicated in the control of Ca^{2+} channel function. The β-subunit tightly binds to a conserved motif within the N-terminal half of the I-II linker. X-ray crystallography and mutational studies (77–79) revealed that an α-helix between the AID (and its bound β-subunit) and IS6 provides a rigid connection to the channel pore and thereby crucially determines the voltage- and Ca^{2+}-dependent gating properties of the channel. In Ca_V2 channels, direct G-protein modulation is also mediated by Gβγ interaction in this region (77, 80). In contrast to this proximal region, no x-ray structure could be obtained C-terminal to the AID in a recent x-ray crystallographic study of the I-II linker in complex with β-subunit (77). Our data suggest that also this portion of the I-II linker forms an α-helix and that its interaction with membrane lipids plays a crucial role in stabilizing the channel conformation. This conformational stabilization may be transmitted either upstream through the I-II linker to the pore (IS6) or downstream through IIS1 to the voltage sensor of the repeat II, or both, and thereby control channel gating.

Based on recent genetic findings that already small changes in LTCC functions underlie human diseases (81), this polybasic motif may also be a target for human disease-causing mutations. Further studies must therefore investigate the consequences of single charge neutralizations within this motif as

well as the role of adjacent positively charged residues for membrane binding and channel function.

References

1. Catterall, W. A. (2011) Voltage-gated calcium channels. *Cold Spring Harb. Perspect. Biol.* **3,** a003947
2. Striessnig, J., Pinggera, A., Kaur, G., Bock, G., and Tuluc, P. (2014) L-type calcium channels in heart and brain. *Wiley Interdiscip. Rev. Membr. Transp. Signal.* **3,** 15–38
3. Liao, P., Yong, T. F., Liang, M. C., Yue, D. T., and Soong, T. W. (2005) Splicing for alternative structures of Cav1.2 calcium channels in cardiac and smooth muscles. *Cardiovasc. Res.* **68,** 197–203
4. Lipscombe, D., Pan, J. Q., and Gray, A. C. (2002) Functional diversity in neuronal voltage-gated calcium channels by alternative splicing of Cavα1. *Mol. Neurobiol.* **26,** 21–44
5. Lipscombe, D. (2005) Neuronal proteins custom designed by alternative splicing. *Curr. Opin. Neurobiol.* **15,** 358–363
6. Peterson, B. Z., DeMaria, C. D., Adelman, J. P., and Yue, D. T. (1999) Calmodulin is the calcium sensor for calcium-dependent inactivation of L-type calcium channels. *Neuron* **22,** 549–558
7. Grueter, C. E., Abiria, S. A., Dzhura, I., Wu, Y., Ham, A. J., Mohler, P. J., Anderson, M. E., and Colbran, R. J. (2006) L-type Ca^{2+} channel facilitation mediated by phosphorylation of the β subunit by CaMKII. *Mol. Cell* **23,** 641–650
8. Hulme, J. T., Westenbroek, R. E., Scheuer, T., and Catterall, W. A. (2006) Phosphorylation of serine 1928 in the distal C-terminal domain of cardiac Cav1.2 channels during β1-adrenergic regulation. *Proc. Natl. Acad. Sci. U.S.A.* **103,** 16574–16579
9. Fu, Y., Westenbroek, R. E., Scheuer, T., and Catterall, W. A. (2014) Basal and β-adrenergic regulation of the cardiac calcium channel Cav1.2 requires phosphorylation of serine 1700. *Proc. Natl. Acad. Sci. U.S.A.* **111,** 16598–16603
10. Doering, C. J., and McRory, J. E. (2007) Effects of extracellular pH on neuronal calcium channel activation. *Neuroscience* **146,** 1032–1043
11. De Waard, M., Liu, H., Walker, D., Scott, V. E., Gurnett, C. A., and Campbell, K. P. (1997) Direct binding of G-protein βγ complex to voltage-dependent calcium channels. *Nature* **385,** 446–450
12. Roberts-Crowley, M. L., Mitra-Ganguli, T., Liu, L., and Rittenhouse, A. R. (2009) Regulation of voltage-gated Ca^{2+} channels by lipids. *Cell Calcium* **45,** 589–601
13. Suh, B. C., and Hille, B. (2008) PIP2 is a necessary cofactor for ion channel function: how and why? *Annu. Rev. Biophys.* **37,** 175–195
14. Wu, L., Bauer, C. S., Zhen, X. G., Xie, C., and Yang, J. (2002) Dual regulation of voltage-gated calcium channels by PtdIns(4,5)P2. *Nature* **419,** 947–952
15. Gamper, N., Reznikov, V., Yamada, Y., Yang, J., and Shapiro, M. S. (2004) Phosphatidylinositol 4,5-bisphosphate signals underlie receptor-specific G$_{q/11}$-mediated modulation of N-type Ca^{2+} channels. *J. Neurosci.* **24,** 10980–10992
16. Suh, B. C., Leal, K., and Hille, B. (2010) Modulation of high-voltage activated Ca^{2+} channels by membrane phosphatidylinositol 4,5-bisphosphate. *Neuron* **67,** 224–238
17. Suh, B. C., Kim, D. I., Falkenburger, B. H., and Hille, B. (2012) Membrane-localized β-subunits alter the PIP2 regulation of high-voltage activated Ca^{2+} channels. *Proc. Natl. Acad. Sci. U.S.A.* **109,** 3161–3166
18. Hermosilla, T., Moreno, C., Itfinca, M., Altier, C., Armisén, R., Stutzin, A., Zamponi, G. W., and Varela, D. (2011) L-type calcium channel β subunit modulates angiotensin II responses in cardiomyocytes. *Channels* **5,** 280–286
19. Roberts-Crowley, M. L., and Rittenhouse, A. R. (2009) Arachidonic acid inhibition of L-type calcium (Cav1.3b) channels varies with accessory Cavβ subunits. *J. Gen. Physiol.* **133,** 387–403
20. Michailidis, I. E., Zhang, Y., and Yang, J. (2007) The lipid connection-regulation of voltage-gated Ca^{2+} channels by phosphoinositides. *Pflugers Arch.* **455,** 147–155
21. Yeung, T., Gilbert, G. E., Shi, J., Silvius, J., Kapus, A., and Grinstein, S. (2008) Membrane phosphatidylserine regulates surface charge and protein localization. *Science* **319,** 210–213
22. Heo, W. D., Inoue, T., Park, W. S., Kim, M. L., Park, B. O., Wandless, T. J., and Meyer, T. (2006) PI(3,4,5)P3 and PI(4,5)P2 lipids target proteins with polybasic clusters to the plasma membrane. *Science* **314,** 1458–1461
23. Hansen, S. B., Tao, X., and MacKinnon, R. (2011) Structural basis of PIP2 activation of the classical inward rectifier K$^+$ channel Kir2.2. *Nature* **477,** 495–498
24. Whorton, M. R., and MacKinnon, R. (2011) Crystal structure of the mammalian GIRK2 K$^+$ channel and gating regulation by G proteins, PIP2, and sodium. *Cell* **147,** 199–208
25. Hille, B., Dickson, E. J., Kruse, M., Vivas, O., and Suh, B. C. (2015) Phosphoinositides regulate ion channels. *Biochim. Biophys. Acta* **1851,** 844–856
26. Altier, C., Garcia-Caballero, A., Simms, B., You, H., Chen, L., Walcher, J., Tedford, H. W., Hermosilla, T., and Zamponi, G. W. (2011) The Cavβ subunit prevents RFP2-mediated ubiquitination and proteasomal degradation of L-type channels. *Nat. Neurosci.* **14,** 173–180
27. Hilgemann, D. W. (2012) Fitting K(V) potassium channels into the PIP(2) puzzle: Hille group connects dots between illustrious HH groups. *J. Gen Physiol.* **140,** 245–248
28. Horton, R. M., Hunt, H. D., Ho, S. N., Pullen, J. K., and Pease, L. R. (1989) Engineering hybrid genes without the use of restriction enzymes: gene splicing by overlap extension. *Gene* **77,** 61–68
29. Long, J. Z., Lackan, C. S., and Hadjantonakis, A. K. (2005) Genetic and spectrally distinct *in vivo* imaging: embryonic stem cells and mice with widespread expression of a monomeric red fluorescent protein. *BMC Biotechnol.* **5,** 20
30. Obermair, G. J., Kugler, G., and Flucher, B. E. (2004) The role of the calcium channel α2 δ-1 subunit in skeletal muscle. *J. Muscle Res. Cell Motil.* **25,** 239–240
31. Obermair, G. J., Schlick, B., Di Biase, V., Subramanyam, P., Gebhart, M., Baumgartner, S., and Flucher, B. E. (2010) Reciprocal interactions regulate targeting of calcium channel β subunits and membrane expression of α$_1$ subunits in cultured hippocampal neurons. *J. Biol. Chem.* **285,** 5776–5791
32. Dayal, A., Bhat, V., Franzini-Armstrong, C., and Grabner, M. (2013) Domain cooperativity in the β1a subunit is essential for dihydropyridine receptor voltage sensing in skeletal muscle. *Proc. Natl. Acad. Sci. U.S.A.* **110,** 7488–7493
33. Campiglio, M., Di Biase, V., Tuluc, P., and Flucher, B. E. (2013) Stable incorporation versus dynamic exchange of β subunits in a native Ca^{2+} channel complex. *J. Cell Sci.* **126,** 2092–2101
34. van der Wal, J., Habets, R., Várnai, P., Balla, T., and Jalink, K. (2001) Monitoring agonist-induced phospholipase C activation in live cells by fluores-

cence resonance energy transfer. *J. Biol. Chem.* **276,** 15337–15344

35. Grabner, M., Dirksen, R. T., and Beam, K. G. (1998) Tagging with green fluorescent protein reveals a distinct subcellular distribution of L-type and non-L-type calcium channels expressed in dysgenic myotubes. *Proc. Natl. Acad. Sci. U.S.A.* **95,** 1903–1908

36. Lindner, M., Leitner, M. G., Halaszovich, C. R., Hammond, G. R., and Oliver, D. (2011) Probing the regulation of TASK potassium channels by PI4,5P(2) with switchable phosphoinositide phosphatases. *J. Physiol.* **589,** 3149–3162

37. Hammond, G. R., Fischer, M. J., Anderson, K. E., Holdich, J., Koteci, A., Balla, T., and Irvine, R. F. (2012) PI4P and PI(4,5)P2 are essential but independent lipid determinants of membrane identity. *Science* **337,** 727–730

38. Ortner, N. J., Bock, G., Vandael, D. H., Mauersberger, R., Draheim, H. J., Gust, R., Carbone, E., Tuluc, P., and Striessnig, J. (2014) Pyrimidine-2,4,6-triones are a new class of voltage-gated L-type Ca²⁺ channel activators. *Nat. Commun.* **5,** 3897

39. Barth, P., Schonbrun, J., and Baker, D. (2007) Toward high-resolution prediction and design of transmembrane helical protein structures. *Proc. Natl. Acad. Sci. U.S.A.* **104,** 15682–15687

40. Yarov-Yarovoy, V., Schonbrun, J., and Baker, D. (2006) Multipass membrane protein structure prediction using Rosetta. *Proteins* **62,** 1010–1025

41. Yarov-Yarovoy, V., Baker, D., and Catterall, W. A. (2006) Voltage sensor conformations in the open and closed states in ROSETTA structural models of K⁺ channels. *Proc. Natl. Acad. Sci. U.S.A.* **103,** 7292–7297

42. Payandeh, J., Scheuer, T., Zheng, N., and Catterall, W. A. (2011) The crystal structure of a voltage-gated sodium channel. *Nature* **475,** 353–358

43. Hildebrand, A., Remmert, M., Biegert, A., and Söding, J. (2009) Fast and accurate automatic structure prediction with HHpred. *Proteins* **77,** 128–132

44. Söding, J., Biegert, A., and Lupas, A. N. (2005) The HHpred interactive server for protein homology detection and structure prediction. *Nucleic Acids Res.* **33,** W244–W248

45. Wang, C., Bradley, P., and Baker, D. (2007) Protein-protein docking with backbone flexibility. *J. Mol. Biol.* **373,** 503–519

46. Yarov-Yarovoy, V., DeCaen, P. G., Westenbroek, R. E., Pan, C. Y., Scheuer, T., Baker, D., and Catterall, W. A. (2012) Structural basis for gating charge movement in the voltage sensor of a sodium channel. *Proc. Natl. Acad. Sci. U.S.A.* **109,** E93–E102

47. Bonneau, R., Strauss, C. E., Rohl, C. A., Chivian, D., Bradley, P., Malmström, L., Robertson, T., and Baker, D. (2002) *De novo* prediction of three-dimensional structures for major protein families. *J. Mol. Biol.* **322,** 65–78

48. Pettersen, E. F., Goddard, T. D., Huang, C. C., Couch, G. S., Greenblatt, D. M., Meng, E. C., and Ferrin, T. E. (2004) UCSF Chimera: a visualization system for exploratory research and analysis. *J. Comput. Chem.* **25,** 1605–1612

49. Gebhart, M., Juhasz-Vedres, G., Zuccotti, A., Brandt, N., Engel, J., Trockenbacher, A., Kaur, G., Obermair, G. J., Knipper, M., Koschak, A., and Striessnig, J. (2010) Modulation of Cav1.3 Ca²⁺ channel gating by Rab3 interacting molecule. *Mol. Cell Neurosci.* **44,** 246–259

50. Takahashi, S. X., Miriyala, J., Tay, L. H., Yue, D. T., and Colecraft, H. M. (2005) A CaVbeta SH3/guanylate kinase domain interaction regulates multiple properties of voltage-gated Ca²⁺ channels. *J. Gen. Physiol.* **126,** 365–377

51. Van Petegem, F., Clark, K. A., Chatelain, F. C., and Minor, D. L., Jr. (2004) Structure of a complex between a voltage-gated calcium channel β-subunit and an α-subunit domain. *Nature* **429,** 671–675

52. Leroy, J., Richards, M. S., Butcher, A. J., Nieto-Rostro, M., Pratt, W. S., Davies, A., and Dolphin, A. C. (2005) Interaction via a key tryptophan in the I-II linker of N-type calcium channels is required for β1 but not for palmitoylated β2, implicating an additional binding site in the regulation of channel voltage-dependent properties. *J. Neurosci.* **25,** 6984–6996

53. Buchan, D. W., Ward, S. M., Lobley, A. E., Nugent, T. C., Bryson, K., and Jones, D. T. (2010) Protein annotation and modelling servers at University College London. *Nucleic Acids Res.* **38,** W563–W568

54. Kadamur, G., and Ross, E. M. (2013) Mammalian phospholipase C. *Annu. Rev. Physiol.* **75,** 127–154

55. Horowitz, L. F., Hirdes, W., Suh, B. C., Hilgemann, D. W., Mackie, K., and Hille, B. (2005) Phospholipase C in living cells: activation, inhibition, Ca²⁺ requirement, and regulation of M current. *J. Gen Physiol.* **126,** 243–262

56. Zahedi, B., Goo, H. J., Beaulieu, N., Tazmini, G., Kay, R. J., and Cornell, R. B. (2011) Phosphoinositide 3-kinase regulates plasma membrane targeting of the Ras-specific exchange factor RasGRP1. *J. Biol. Chem.* **286,** 12712–12723

57. Bae, Y. S., Lee, T. G., Park, J. C., Hur, J. H., Kim, Y., Heo, K., Kwak, J. Y., Suh, P. G., and Ryu, S. H. (2003) Identification of a compound that directly stimulates phospholipase C activity. *Mol. Pharmacol.* **63,** 1043–1050

58. Várnai, P., and Balla, T. (1998) Visualization of phosphoinositides that bind pleckstrin homology domains: calcium- and agonist-induced dynamic changes and relationship to myo-[³H]inositol-labeled phosphoinositide pools. *J. Cell Biol.* **143,** 501–510

59. Fuller, M. D., Emrick, M. A., Sadilek, M., Scheuer, T., and Catterall, W. A. (2010) Molecular mechanism of calcium channel regulation in the fight-or-flight response. *Sci. Signal.* **3,** ra70

60. Hulme, J. T., Konoki, K., Lin, T. W., Gritsenko, M. A., Camp, D. G., 2nd, Bigelow, D. J., and Catterall, W. A. (2005) Sites of proteolytic processing and noncovalent association of the distal C-terminal domain of Cav1.1 channels in skeletal muscle. *Proc. Natl. Acad. Sci. U.S.A.* **102,** 5274–5279

61. Hulme, J. T., Yarov-Yarovoy, V., Lin, T. W., Scheuer, T., and Catterall, W. A. (2006) Autoinhibitory control of the Cav1.2 channel by its proteolytically processed distal C-terminal domain. *J. Physiol.* **576,** 87–102

62. Lieb, A., Scharinger, A., Sartori, S., Sinnegger-Brauns, M. J., and Striessnig, J. (2012) Structural determinants of CaV1.3 L-type calcium channel gating. *Channels* **6,** 197–205

63. Singh, A., Gebhart, M., Fritsch, R., Sinnegger-Brauns, M. J., Poggiani, C., Hoda, J. C., Engel, J., Romanin, C., Striessnig, J., and Koschak, A. (2008) Modulation of voltage- and Ca²⁺-dependent gating of Cav1.3 L-type calcium channels by alternative splicing of a C-terminal regulatory domain. *J. Biol. Chem.* **283,** 20733–20744

64. Cao, Y., Bartolomé-Martín, D., Rotem, N., Rozas, C., Dellal, S. S., Chacon, M. A., Kadriu, B., Gulinello, M., Khodakhah, K., and Faber, D. S. (2015) Rescue of homeostatic regulation of striatal excitability and locomotor activity in a mouse model of Huntington's disease. *Proc. Natl. Acad. Sci. U.S.A.* **112,** 2239–2244

65. Hall, D. D., Dai, S., Tseng, P.-Y., Malik, Z., Nguyen, M., Matt, L., Schnizler, K., Shephard, A., Mohapatra, D. P., Tsuruta, F., Dolmetsch, R. E., Christel, C. J., Lee, A., Burette, A., Weinberg, R. J., and Hell, J. W. (2013) Competition between α-actinin and Ca²⁺-calmodulin controls surface retention of the L-type Ca²⁺ channel Cav1.2. *Neuron* **78,** 483–497

66. Rhee, S. G., and Choi, K. D. (1992) Multiple forms of phospholipase C isozymes and their activation mechanisms. *Adv. Second Messenger Phosphoprotein Res.* **26,** 35–61

67. Miranda-Laferte, E., Ewers, D., Guzman, R. E., Jordan, N., Schmidt, S., and Hidalgo, P. (2014) The N-terminal domain tethers the voltage-gated calcium channel β2e-subunit to the plasma membrane via electrostatic and hydrophobic interactions. *J. Biol. Chem.* **289,** 10387–10398

68. Gonzalez-Gutierrez, G., Miranda-Laferte, E., Contreras, G., Neely, A., and Hidalgo, P. (2010) Swapping the I-II intracellular linker between L-type Cav1.2 and R-type Cav2.3 high-voltage gated calcium channels exchanges activation attributes. *Channels* **4,** 42–50

69. Neely, A., and Hidalgo, P. (2014) Structure-function of proteins interacting with the α1 pore-forming subunit of high-voltage-activated calcium channels. *Front. Physiol.* **5,** 209

70. Zhen, X. G., Xie, C., Yamada, Y., Zhang, Y., Doyle, C., and Yang, J. (2006) A single amino acid mutation attenuates rundown of voltage-gated calcium channels. *FEBS Lett.* **580,** 5733–5738

71. Rousset, M., Cens, T., Gouin-Charnet, A., Scamps, F., and Charnet, P. (2004) Calcium and phosphatidylinositol 4,5-bisphosphate stabilize a Gβγ-sensitive state of Ca V2 Ca²⁺ channels. *J. Biol. Chem.* **279,** 14619–14630

72. Yang, Y. R., Follo, M. Y., Cocco, L., and Suh, P. G. (2013) The physiological roles of primary phospholipase C. *Adv. Biol. Regul.* **53,** 232–241

73. Rhee, S. G., and Bae, Y. S. (1997) Regulation of phosphoinositide-specific phospholipase C isozymes. *J. Biol. Chem.* **272,** 15045–15048

74. Suh, P. G., Park, J. I., Manzoli, L., Cocco, L., Peak, J. C., Katan, M., Fukami, K., Kataoka, T., Yun, S., and Ryu, S. H. (2008) Multiple roles of phosphoinositide-specific phospholipase C isozymes. *BMB Rep.* **41,** 415–434

75. Balasubramanian, K., Mirnikjoo, B., and Schroit, A. J. (2007) Regulated externalization of phosphatidylserine at the cell surface: implications for apoptosis. *J. Biol. Chem.* **282,** 18357–18364

76. Suh, B. C., and Hille, B. (2002) Recovery from muscarinic modulation of M current channels requires phosphatidylinositol 4,5-bisphosphate synthesis. *Neuron* **35,** 507–520

77. Almagor, L., Chomsky-Hecht, O., Ben-Mocha, A., Hendin-Barak, D., Dascal, N., and Hirsch, J. A. (2012) The role of a voltage-dependent Ca^{2+} channel intracellular linker: a structure-function analysis. *J. Neurosci.* **32,** 7602–7613

78. Baumgart, J. P., Vitko, I., Bidaud, I., Kondratskyi, A., Lory, P., and Perez-Reyes, E. (2008) I-II loop structural determinants in the gating and surface expression of low voltage-activated calcium channels. *PLoS One* **3,** e2976

79. Findeisen, F., and Minor, D. L., Jr. (2009) Disruption of the IS6-AID linker affects voltage-gated calcium channel inactivation and facilitation. *J. Gen. Physiol.* **133,** 327–343

80. Tedford, H. W., Kisilevsky, A. E., Vieira, L. B., Varela, D., Chen, L., and Zamponi, G. W. (2010) Scanning mutagenesis of the I-II loop of the Cav2.2 calcium channel identifies residues arginine 376 and valine 416 as molecular determinants of voltage dependent G protein inhibition. *Mol. Brain* **3,** 6

81. Pinggera, A., Lieb, A., Benedetti, B., Lampert, M., Monteleone, S., Liedl, K. R., Tuluc, P., and Striessnig, J. (2015) CACNA1D *de novo* mutations in autism spectrum disorders activate Cav1.3 L-type calcium channels. *Biol. Psychiatry* **77,** 816–822